

## PHYSICAL CONDITIONS IN THE NARROW-LINE REGION OF M51<sup>1</sup>

L. D. BRADLEY, M. E. KAISER

Department of Physics and Astronomy, The Johns Hopkins University,  
 3400 N. Charles Street, Baltimore, MD 21218

AND

W. A. BAAN

ASTRON, Westerbork Observatory, PO Box 2, Dwingeloo, 7990 AA, The Netherlands

Received 2003 September 30; accepted 2003 November 24

### ABSTRACT

We have investigated the physical conditions in the narrow-line region (NLR) of M51 using long-slit spectra obtained with the Space Telescope Imaging Spectrograph (STIS) aboard the *Hubble Space Telescope* (*HST*) and 3.6 cm radio continuum observations obtained with the Very Large Array (VLA)<sup>2</sup>. Emission-line diagnostics were employed for nine NLR clouds, which extend 2''.5 (102 pc) from the nucleus, to examine the electron density, temperature, and ionization state of the NLR gas. The emission-line ratios are consistent with those typically found in Seyfert nuclei and indicate that within the inner near-nuclear region ( $r \lesssim 1''$ ) the ionization decreases with increasing radius. Upper-limits to the [O III] electron temperature ( $T_e \lesssim 11,000$  K) for the inner NLR clouds indicate that photoionization is the dominant ionization mechanism close to the nucleus. The emission-line fluxes for most of the NLR clouds can be reproduced reasonably well by simple photoionization models using a central power-law continuum source and supersolar nitrogen abundances. Shock+precursor models, however, provide a better fit to the observed fluxes of an NLR cloud  $\sim 2''.5$  south of the nucleus that is identified with the extra-nuclear cloud (XNC). The large [O III] electron temperature of this cloud ( $T_e = 24,000$  K) further suggests the presence of shocks. This cloud is straddled by two radio knots and lies near the location where a weak radio jet,  $\sim 2''.5$  (102 pc) in extent, connects the near-nuclear radio emission with a diffuse lobe structure spanning  $\sim 4''$  (163 pc). It is plausible that this cloud represents the location where the radio jet impinges on the disk ISM.

*Subject headings:* galaxies: active — galaxies: individual (M51) — galaxies: nuclei — galaxies: Seyfert

### 1. INTRODUCTION

Photoionization by a central source is widely regarded as the dominant process responsible for producing the emission-line spectra observed in the Narrow-Line Region (NLR) of Seyfert galaxies. Support for these photoionization models is provided by their general success in reproducing the observed ultraviolet (UV) and optical emission line spectra (e.g. Ferland & Osterbrock 1986) and by the observed biconical morphology present in many Seyfert galaxies, which is suggestive of collimation by a central ionizing source.

Many of these Seyfert galaxies also possess radio emission, which appears collimated and extended, with similar orientation, on the same scale as the optical emission. The radio power has been shown to be correlated with the [O III] luminosity and full-width half-maximum (FWHM) (de Bruyn & Wilson 1978; Heckman et al. 1981; Whittle 1985, 1992). High spatial resolution imaging of the NLR often illustrates a more detailed correspondence between the radio knots and the optical emission-line clouds (Pogge & de Robertis 1995; Capetti et al. 1996; Falcke et al. 1998).

While photoionization models assuming a central ionizing source are generally successful in reproducing the observed emission-line spectra, there are some indications that other

processes may also contribute. Simple photoionization models, in some cases, underpredict the electron temperature in the gas (determined from the [O III]  $(\lambda 4959 + \lambda 5007)/\lambda 4363$  line ratio) and are not always able to explain strong UV emission from intermediate excitation line species, such as C III] and C IV (Ferland & Osterbrock 1986). Thus, the complex velocity distribution presented by some Seyferts (Cecil 1988; Whittle et al. 1988; Winge et al. 1997; Hutchings et al. 1998) and the aforementioned optical-radio correspondence suggests that another process, such as shocks, may contribute to the observed emission-line spectrum. The role of shocks in the NLR provides a key to the understanding the relative importance of mechanical versus radiative energy processes in the active galactic nuclei (AGN) model.

We examine the physical conditions influencing the NLR kinematics and ionization structure, in particular the relative importance of photoionization and shocks within the NLR of M51. M51 (NGC 5194) is a nearby (8.4 Mpc, Feldmeier et al. 1997), nearly face-on, Sbc grand-design spiral galaxy that hosts a weak active nucleus. Early observations attributed the ionization structure in the nuclear region to photoionization by the active nucleus (Rose & Searle 1982; Rose & Cecil 1983). However, later observations revealed structures that indicated shocks also may be an important source of ionization in this object (Ford et al. 1985; Cecil 1988). In particular, shocks were postulated to be the dominant energy mechanism exciting the emission-line gas in an extended extra-nuclear cloud (XNC) lying  $\sim 3''$  south of the nucleus.

Several factors led to this conclusion for the XNC. Ford et al. (1985) observed high electron temperatures determined from line-ratio diagnostics, emission-line ratios qual-

<sup>1</sup> Based on observations made with the NASA/ESA *Hubble Space Telescope*, obtained at the Space Telescope Science Institute, which is operated by the Association of Universities for Research in Astronomy under NASA contract NAS5-26555.

<sup>2</sup> The VLA is a facility of the National Radio Astronomy Observatory, which is operated by Associated Universities, Inc., under cooperative agreement with the National Science Foundation.

itatively similar to that observed in supernova remnants, a limb brightened morphology, and abrupt changes in the spectral characteristics between the galactic disk and the XNC cloud. Further, Cecil (1988) found sharply-defined high-velocity emission structures that resembled the termini of hydrodynamic flows and the broadest emission lines localized along the northern boundary of the XNC. A directed nuclear outflow interacting with the disk of M51 was postulated as the source of the shocks in the XNC.

Direct evidence for a weak radio jet connecting the nuclear radio emission with the southern extra-nuclear emission was provided by 4.8 GHz observations obtained with the Very Large Array (VLA) (Crane & van der Hulst 1992). An extended lobe structure that is morphologically similar to the optical XNC emission also is observed in the radio map at this frequency. A lower brightness halo engulfs the nucleus, the jet, and regions north of the nucleus.

Recent *Chandra* observations ( $\sim 1''$  resolution) by Terashima & Wilson (2001) show an extended X-ray morphology for the XNC that is similar to both the optical and radio data. The X-ray data further support the argument for shocks in the XNC. These authors modelled the X-ray spectra of this region with a thermal plasma resulting from shock-heating due to outflows. Their model yielded a X-ray temperature  $T_X = 6.7 \times 10^6$  K for the XNC, which corresponds to a shock velocity of  $690 \text{ km s}^{-1}$ . This value is roughly consistent with the  $\sim 500 \text{ km s}^{-1}$  shock velocity previously inferred by Cecil (1988).

In this paper, we examine the physical conditions influencing the NLR kinematics and ionization structure, in particular the relative importance of photoionization and shocks within the NLR of M51. In § 2 we present the observations, data reduction, and stellar background subtraction. In § 3 we present the optical morphology, cloud kinematics, emission-line ratios, and physical conditions within the NLR gas. In § 4 we present our VLA 8.4 GHz radio observations and compare them with archival *Hubble Space Telescope* (*HST*) Wide Field and Planetary Camera (WFPC2) optical images. We discuss the photoionization modelling of the NLR clouds in § 5, and discuss ionizing shock models in § 6. Our results are summarized in § 7, and our conclusions are presented in § 8.

Given the distance to M51 of 8.4 Mpc (Feldmeier et al. 1997),  $1''$  corresponds to 40.7 pc.

## 2. OBSERVATIONS

High spatial resolution ( $0.''1$ , 4.1 pc) long-slit spectra of the nuclear region of M51 were obtained with the Space Telescope Imaging Spectrograph (STIS) aboard *HST*. The spectra were acquired through a  $52'' \times 0.''2$  slit oriented at a single position angle of  $166^\circ$  (E of N). This position angle was based on our analysis of an archival *HST*/WFPC2 F502N narrowband image of the near-nuclear region of M51 and was selected to intersect the nucleus and several of the brightest NLR clouds at this wavelength. The low-dispersion grating modes G430L (Fig. 1) and G750L (Fig. 2) were used to provide continuous wavelength coverage spanning the spectral region from  $2900 \text{ \AA}$  to  $1 \mu\text{m}$ . The  $0.''2$  wide slit ( $0.''19$  as-built width) projects onto 3.75 STIS CCD pixels (1.9 resolution elements) and corresponds to spectral resolutions of  $10.3 \text{ \AA}$  for G430L and  $18.3 \text{ \AA}$  for G750L. The associated velocity resolutions for this slit are  $827 \text{ km s}^{-1}$  at  $[\text{O II}] \lambda\lambda 3727$ ,  $615 \text{ km s}^{-1}$  at  $[\text{O III}] \lambda 5007$ , and  $834 \text{ km s}^{-1}$  at  $\text{H}\alpha$ .

To determine the sub-arcsecond velocity structure of the

emission-line clouds, we observed the spectral region containing  $\text{H}\beta$ ,  $[\text{O III}] \lambda 4959$ , and  $[\text{O III}] \lambda 5007$  with the G430M ( $\lambda_c = 4961 \text{ \AA}$ ) medium-dispersion grating mode (Fig. 3). The spectral resolution of this data is  $1.0 \text{ \AA}$ , which corresponds to  $62 \text{ km s}^{-1}$  at  $[\text{O III}] \lambda 5007$ .

In addition, we have observed M51 with the VLA in A-array at 8.46 GHz (3.6 cm) on 14 August 1999. During the data reduction procedure in AIPS, the data were thoroughly flagged in order to remove the effects of a severe lightning storm that passed over the western arm during the latter part of the observations. Four representations of the radio data of the central region of M51 are presented in Figure 4.

A large scale map of the central region (Fig. 4a) displays two prominent sources: the nuclear source with an extended lobe structure toward the south, and an elongated source at  $27.''8$  to the northwest at  $\text{P.A.} = 335^\circ$ . The resolution of this naturally weighted map is  $0.''99 \times 0.''79$  and has a rms noise of  $13 \mu\text{Jy/beam}$ . Higher resolution maps are presented of both sources. The naturally weighted map of the nuclear source (Fig. 4b) has a resolution of  $0.''29 \times 0.''26$  and a rms noise of  $8 \mu\text{Jy/beam}$ . The uniformly weighted map of the nucleus (Fig. 4d) has a resolution of  $0.''18 \times 0.''15$  and a rms noise of  $10 \mu\text{Jy/beam}$ . While the naturally weighted map shows the nuclear source together with the southern jet and the extended radio lobe, the uniformly weighted map only shows the nuclear source and the inner part of the southern jet. The peak flux density of the nuclear source in the two maps is  $210 \mu\text{Jy/beam}$  and  $195 \mu\text{Jy/beam}$ , respectively.

The discrete northern source in the nuclear region of M51 consists of three compact components and is presented in Figure 4c. The resolution of this naturally weighted map is  $0.''29 \times 0.''26$  and has a rms noise of  $8.6 \mu\text{Jy/beam}$ .

A log of the optical and radio observations is presented in Table 1, which includes the archival *HST*/WFPC2 (Ford et al. 1996) and VLA 6 cm (Crane & van der Hulst 1992) data.

### 2.1. Data Reduction

The images and spectra were reduced using the IDL CAL-STIS pipeline developed for the STIS Instrument Development Team (IDT). Cosmic rays were removed from the data by combining all of the observations in a given spectroscopic mode using an iterative sigma-clipping algorithm based on a calibrated noise model of the images. After subtracting the detector bias and superdark frames, pixel-to-pixel variations in the CCD response were removed from the G430L and G430M spectra with the standard pipeline flat-field images. A contemporaneous flat-field image was used to remove the fringing in the G750L spectral image at wavelengths longer than  $7000 \text{ \AA}$ .

The data were wavelength calibrated using exposures of an onboard Pt/Cr-Ne spectral line lamp to determine the wavelength zero-point offsets to the pipeline dispersion coefficients. Geometric rectification of the images provided a constant wavelength along each column of the spectral images. Using the pipeline sensitivity tables, the data were flux-calibrated in units of  $\text{erg s}^{-1} \text{ cm}^{-2} \text{ \AA}^{-1}$  per cross-dispersion pixel.

Residual hot pixels present in featureless regions of the post-pipeline processed spectral images were removed using an iterative  $\sigma$ -clipping procedure. A  $1 \times 51$  pixel boxcar was passed over these regions, and successive filtering iterations were performed beginning with  $8\sigma$  and cleaning down to a  $3\sigma$  threshold.

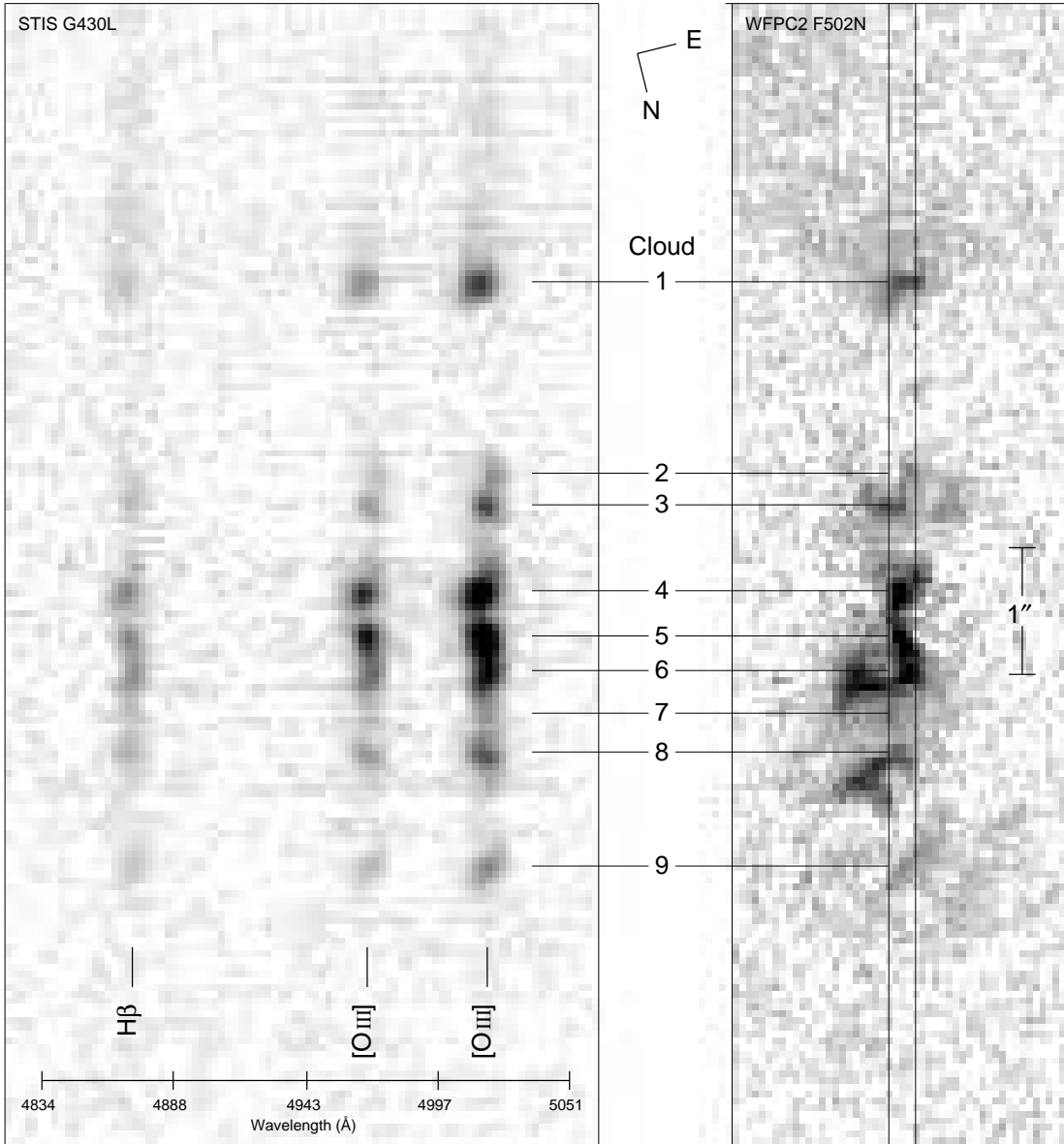


FIG. 1.— (left)  $\text{H}\beta$ ,  $[\text{OIII}] \lambda 4959$ , and  $[\text{OIII}] \lambda 5007$  emission lines extracted from the background-subtracted *HST*/STIS G430L spectral image (see Table 1 for details) of the near-nuclear region of M51. The total spatial extent is  $8.''6$  (350 pc), and the wavelength scale is in the observed frame. (right) Continuum-subtracted *HST*/WFPC2 F502N narrowband  $[\text{OIII}]$  image that has been rotated to the STIS position angle ( $166^\circ$ ) and resampled to the STIS plate scale ( $0.''051 \text{ pixel}^{-1}$ ). The location of the STIS  $52'' \times 0.''2$  slit is overplotted on the WFPC2 image. The NLR clouds have been labeled for identification in both images.

The background present in the medium spectral resolution G430M image consists of the near-nuclear stellar continuum of the M51 host galaxy, which fills the entire length of the STIS slit. Because changes in the continuum shape are small ( $\sim 5\%$ ) over the narrow G430M spectral range (282 Å), we removed the background using an empirical cross-dispersion template of the spectral image in regions without emission features. After masking the emission-line clouds, the background template was generated by calculating the median of each image row. The cross-dispersion template was then subtracted from each column of the spectral image.

Nine spatially resolved emission-line clouds were identified in the data (see Figures 1 and 2). Individual cloud spectra were created by adding adjacent rows along the slit in the spatial direction. The number of summed rows (typically three pixels,  $0.''15$ ) varied from cloud to cloud and was chosen

based on the spatial extent of the  $[\text{OII}] \lambda\lambda 3727$  emission line.

## 2.2. *G430L and G750L Host Galaxy Subtraction*

Because the active nucleus of M51 is obscured, which is expected for a Seyfert 2 galaxy, the AGN continuum is not apparent in our lower resolution G430L and G750L spectra. However, the near-nuclear spectra exhibit a strong stellar spectrum from the M51 host galaxy. Since the  $\text{H}\beta$ ,  $\text{H}\gamma$ , and  $\text{H}\delta$  spectral features are comprised of both emission and absorption lines, accurate measurement and subtraction of the stellar components is important for accurately measuring the emission-line flux. This is also true for several other emission lines (e.g.  $[\text{NeIII}] \lambda 3869$ ) that have nearby stellar absorption features.  $\text{H}\alpha$  absorption is not directly observed due to the strong adjacent  $[\text{NII}] \lambda\lambda 6548, 6583$  emission lines. However, the presence of  $\text{H}\beta$  stellar absorption suggests that  $\text{H}\alpha$

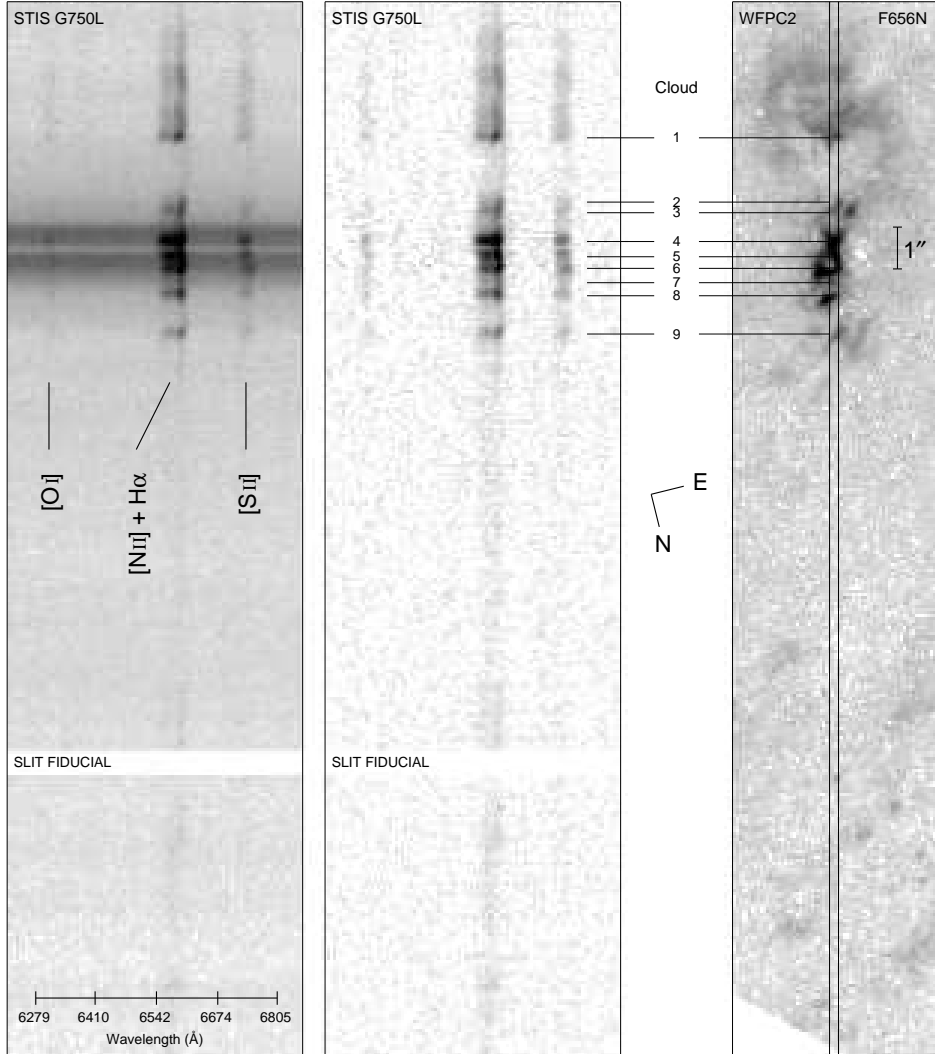


FIG. 2.— (left)  $[\text{O I}] \lambda\lambda 6300, 6364$ ,  $[\text{N II}] \lambda\lambda 6548, 6583$ ,  $\text{H}\alpha$ , and  $[\text{S II}] \lambda\lambda 6716, 6731$  emission lines extracted from the *HST/STIS G750L* spectral image (see Table 1 for details) of the near-nuclear region of M51. The total spatial extent is  $23.^{\circ}6$  (960 pc), and the wavelength scale is in the observed frame. Note the extended  $[\text{N II}] + \text{H}\alpha$  emission to the north of the nucleus. (middle) Background-subtracted version of the spectral image at left. (right) Continuum-subtracted *HST/WFPC2 F656N* narrowband  $[\text{N II}] + \text{H}\alpha$  image that has been rotated to the STIS position angle ( $166^{\circ}$ ) and resampled to the STIS plate scale ( $0.^{\circ}051 \text{ pixel}^{-1}$ ). The location of the STIS  $52'' \times 0.^{\circ}2$  slit is overplotted on the WFPC2 image. The NLR clouds have been labeled for identification in both images.

absorption also is present. Measurement of the  $\text{H}\alpha$  and  $\text{H}\beta$  stellar absorption features is especially important because the  $\text{H}\alpha/\text{H}\beta$  Balmer decrement is used as our reddening indicator. The removal of the stellar background is complicated by the presence of variable extinction in the near-nuclear region. The variable reddening changes the continuum shape of the spectra and adds an additional degeneracy to the well known age-metallicity degeneracy. If continuum shape alone was used as a fit diagnostic, then a highly reddened spectrum could mimic an older stellar population. Thus, the stellar population background must fit both the continuum shape and the stellar absorption lines.

To determine the stellar background in the near-nuclear region of M51, we performed a population synthesis on our least extinguished (bluest) cloud spectrum in the inner nuclear region. This cloud (cloud 6) is  $0.^{\circ}43$  from the obscured nucleus. It is less extinguished than clouds 4 and 5, and exhibits very little differential extinction across its spatial extent. We did not expect a stellar population gradient within the near-nuclear region ( $\sim 1''$ , 41 pc) nor did we see evidence in the

WFPC2 images for localized star formation. Consequently, cloud 6 was used to determine our stellar population template in the near-nuclear region. To increase the signal-to-noise in the spectrum, we combined all four rows ( $0.^{\circ}2$ ) of cloud 6 before performing the stellar population synthesis. Assuming an invariant intrinsic stellar population within the near-nuclear region, the only free parameters in fitting the remaining emission-line clouds are the reddening,  $E(B-V)$ , and an overall multiplicative scale factor.

The first step in the process was to separate the stellar and emission-line contributions to the observed NLR spectrum. In the case where the emission line occurs in an otherwise featureless spectral region, we excluded the emission line from the stellar population fit. In regions where the emission from the active nucleus is superimposed upon stellar features, we simultaneously fit the absorption and emission components using the SPECFIT procedure in IRAF<sup>3</sup>. These fits were per-

<sup>3</sup> IRAF is distributed by the National Optical Astronomy Observatories, which is operated by the Association of Universities for Research in Astron-

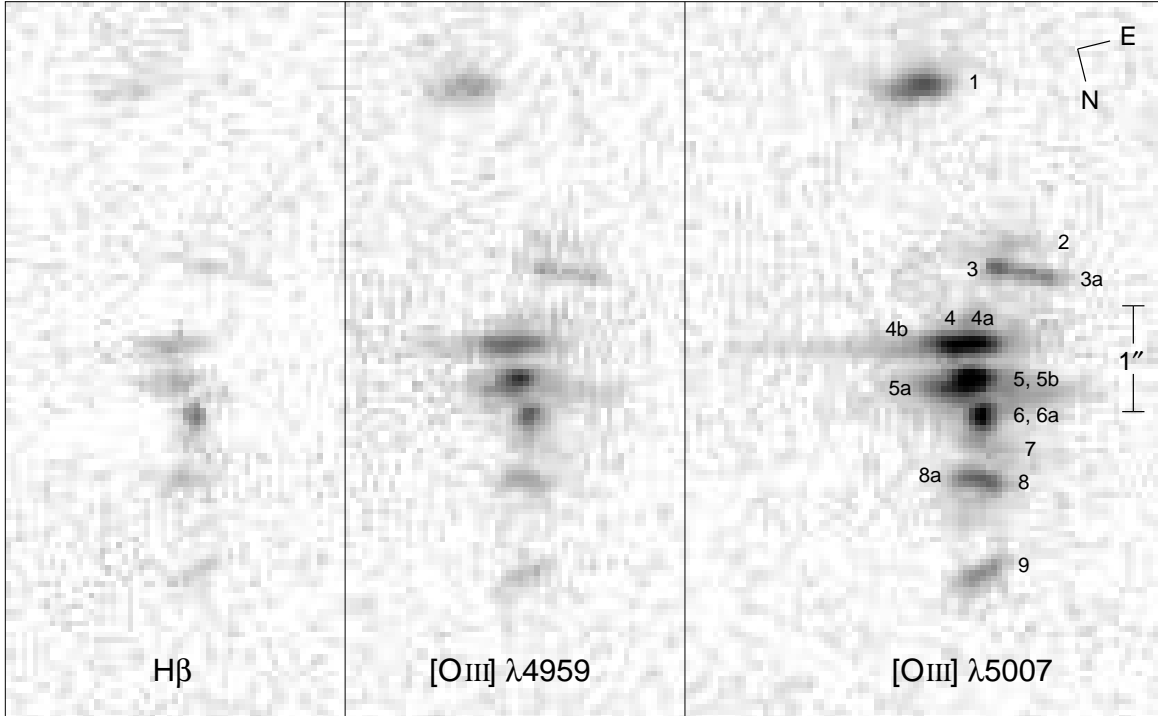


FIG. 3.—Spectral cuts of the H $\beta$ , [OIII]  $\lambda$ 4959, and [OIII]  $\lambda$ 5007 emission lines extracted from the background-subtracted *HST*/STIS G430M spectral image (see Table 1 for details). The clouds are labeled for identification. Clouds with multiple components have the lower-case letters “a” and “b” appended to their cloud labels.

TABLE 1. M51 JOURNAL OF OBSERVATIONS

Date	Instrument	Filter	Aperture	Grating	$\lambda_c$ (Å or cm)	$\Delta\lambda$ (Å or cm)	Exposure Time (s or hr)
Optical Data							
1995 Jan 24 <sup>a</sup>	WFPC2	F502N			5012	26.9	1700
1995 Jan 24 <sup>a</sup>	WFPC2	F547M			5446	486.6	860
1995 Jan 24 <sup>a</sup>	WFPC2	F656N			6564	21.5	1800
1998 Apr 3	STIS	Clear	50CCD		5852	4410	30
1998 Apr 3	STIS	Clear	52'' $\times$ 0''.2		5852	4410	30
1998 Apr 3	STIS	Clear	52'' $\times$ 0''.2	G430L	4300	2807	3086
1998 Apr 3	STIS	Clear	52'' $\times$ 0''.2	G430M	4961	282	2458
1998 Apr 3	STIS	Clear	52'' $\times$ 0''.2	G750L	7751	4987	1644
Radio Data							
1985 Jan 27 <sup>b</sup>	VLA-A				6 cm	0.13 cm	12 hr
1986 May 9-10 <sup>b</sup>	VLA-A				6 cm	0.13 cm	12 hr
1986 May 11-12 <sup>b</sup>	VLA-A				6 cm	0.13 cm	12 hr
1986 May 15-16 <sup>b</sup>	VLA-A				6 cm	0.13 cm	12 hr
1999 Aug 14	VLA-A				3.6 cm	0.04 cm	10 hr

<sup>a</sup>Archival data (Ford et al. 1996).

<sup>b</sup>Archival data (Crane & van der Hulst 1992).

formed on a line-by-line basis for the spectral region encompassing the absorption and emission lines. A Gaussian profile was used for the absorption, while the [OIII]  $\lambda$ 5007 emission-line profile was used as a template for the emission. The resulting absorption fit was inserted into the spectral region of these two-component features.

The spectral synthesis fit was then performed on the “stellar” spectra using a reddened (Fitzpatrick 1999) linear combination of empirical stellar templates (Pickles 1998). The

omy, Inc., under cooperative agreement with the National Science Foundation.

Pickles (1998) stellar library was selected over the Kurucz (1993), Silva & Cornell (1992), and Bica & Alloin (1986) libraries due to its complete wavelength coverage, 10 Å resolution, extensive stellar types, and the superiority of the resulting fit. The 131 spectra in the Pickles stellar library spanned all luminosity classes and included both metal-weak and metal-rich giants. The stellar synthesis represented the best linear combination of the Pickles empirical stellar templates plus an overall reddening correction.

To partially constrain the population synthesis, we used the results of Panagia et al. (1996) on the dust and stellar content in the nuclear region of M51. Panagia et al. (1996)

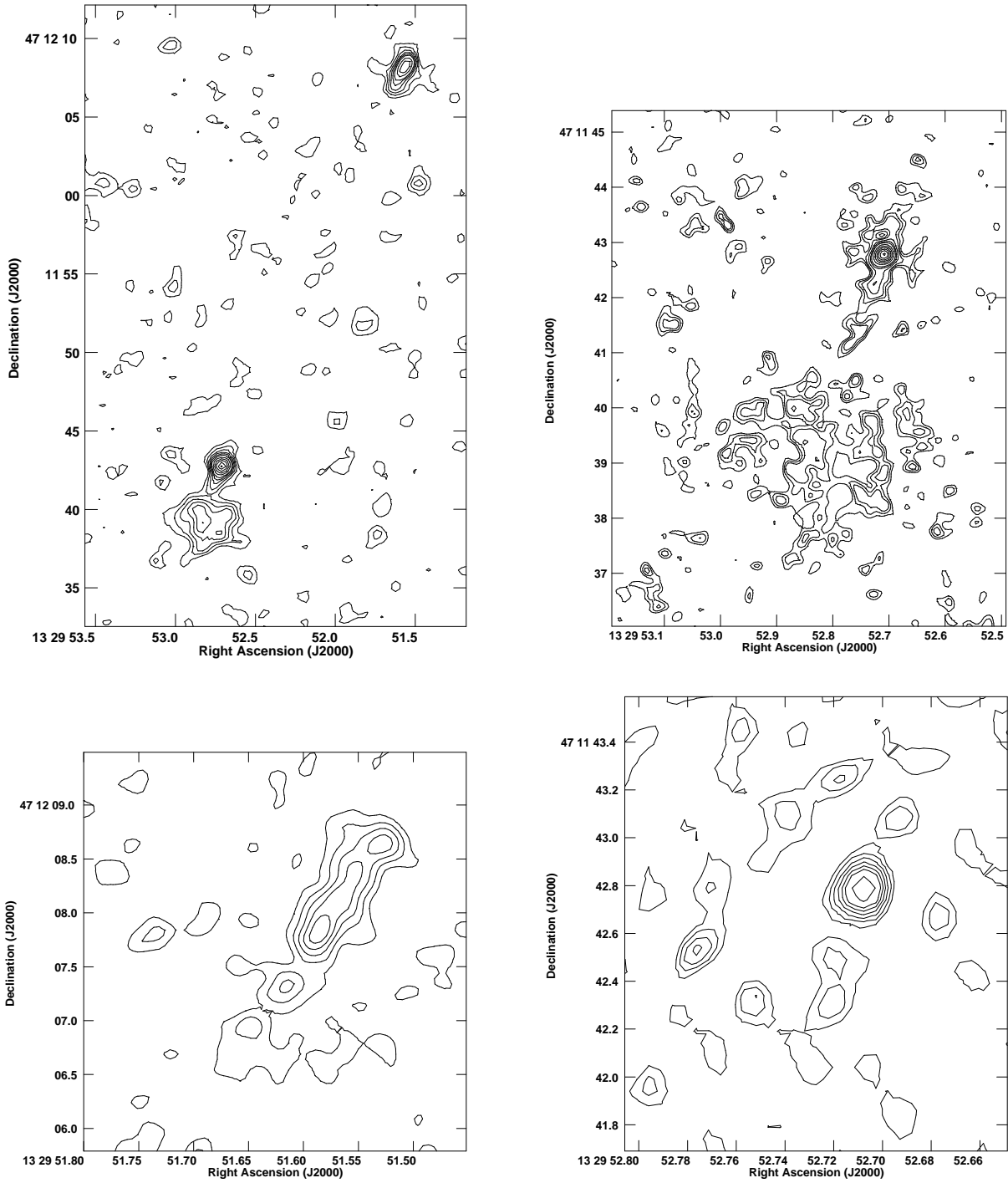


FIG. 4.— Radio structure in the nuclear region of M51 at 3.6 cm with the VLA-A. (a) (top left) The large scale nuclear structure in a naturally weighted map at a resolution of  $0''.99 \times 0''.79$  and a rms noise of 13  $\mu\text{Jy}/\text{beam}$ . The contour levels are at  $[2,4,6,8,10,12,16,20,24,28,32,36,40] \times 10 \mu\text{Jy}/\text{beam}$ . (b) (top right) Naturally weighted map of the nuclear region with contour levels at  $[2,4,6,8,10,12,16,20,24,28,32,36,40] \times 7.5 \mu\text{Jy}/\text{beam}$ . The angular resolution is  $0''.29 \times 0''.26$  and the rms noise is 8  $\mu\text{Jy}/\text{beam}$ . (c) (bottom left) Naturally weighted map of the northern source. The contour levels are the same as in (b). The peak flux densities of the sources, from north to south, are 64, 68, and 79  $\mu\text{Jy}/\text{beam}$ . (d) (bottom right) Uniformly weighted map of the nucleus at a resolution of  $0''.18 \times 0''.15$ . The rms noise is 10  $\mu\text{Jy}/\text{beam}$  and the contour levels are the same as in (a).

found that the stellar population in the near-nuclear “core” of M51 ( $r \lesssim 1''$ ) has a main-sequence turnoff around A0 (age  $\gtrsim 400$  Myr), while the stellar population in the bulge ( $r \gtrsim 1''$ ) has a main-sequence turnoff near G0 (age  $\gtrsim 8$  Gyrs). Thus, for the spectral synthesis on cloud 6 ( $r = 0.''43$ ) we excluded O and B main-sequence stars.

Before performing the stellar population fit, we normalized the NLR cloud spectra at 5556 Å to match the normalization of the stellar templates. It was unnecessary to broaden the absorption features in the stellar templates since the stellar velocity dispersion in the near-nuclear region of M51 (62 km s<sup>-1</sup>, Delisle & Hardy 1992) is negligible compared to our spectra resolution (615 km s<sup>-1</sup> at [O III]  $\lambda 5007$ ) and that of the stellar templates (600 km s<sup>-1</sup> at [O III]  $\lambda 5007$ ). The NaID absorption feature is contaminated by foreground Galactic absorption (Kormendy et al. 1996; Vaceli et al. 1997) and was excluded from the stellar population fit.

The resulting best fit for cloud 6 (Fig. 5) yields a stellar  $E(B-V)$  of 0.09 and a  $\chi^2_{\nu} = 0.52$  ( $\nu = 1506$ ). The lower portion of Fig. 5 shows the cloud 6 spectrum after the stellar background was removed. The background-subtracted spectrum shows very little residual stellar structure with the exception of NaID. The NaID feature does not impact our data because we do not observe any emission lines in this region of the spectrum.

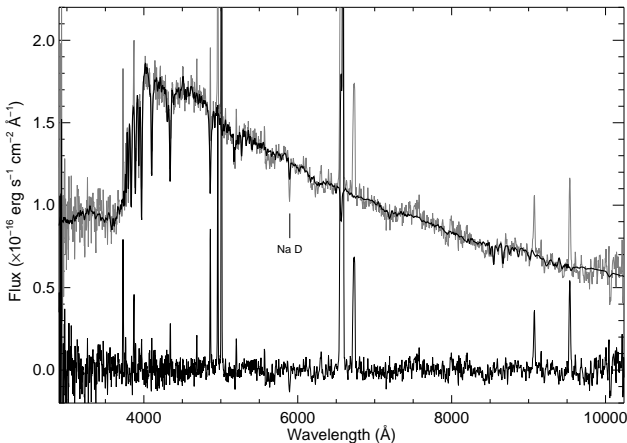


FIG. 5.— Observed cloud 6 spectrum overplotted with the stellar population fit (thick black line) used to subtract the underlying stellar continuum. The bottom spectrum shows the results of the background subtraction.

Comparing the stellar population fit to the near-nuclear NLR clouds showed that the stellar composition appears constant within  $r \lesssim 1''$  (41 pc, clouds 3–7). Therefore, we fit the cloud 6 composite stellar template to the NLR cloud spectra within this region by varying the reddening of the stellar template and multiplying it by an overall scale factor.

Because clouds 4 and 5 exhibit variable reddening across their spatial extents (5 pixels, 0.''25), each of these clouds was split into two cloudlets: one that represented the co-addition of two rows, and the other the co-addition of three rows. The spectra were binned in the spatial direction to both increase the signal-to-noise and to perform the measurement on the scale of a spatial resolution element (2 pixels, 0.''1). All other emission-line clouds were summed over their full spatial extents (typically three pixels, 0.''15) before fitting.

While the stellar composition appears constant within the central radius of  $\sim 1''$  (41 pc), the near-nuclear stellar popula-

tion template provides a poorer fit to the NLR clouds at radii  $\gtrsim 1''$ . From inspection of the stellar background as a function of radius, the relative strengths of the Balmer absorption lines decrease while the Ca II and metal (e.g. TiO and MgH) absorption lines increase, indicating an increased contribution from an older stellar population outside the near-nuclear region. Consequently, we performed a new stellar population synthesis for clouds 2 and 8 ( $r \gtrsim 1''$ ). Again using the results of Panagia et al. (1996), we excluded main-sequence stars earlier than G0 in the spectral synthesis of clouds 2 and 8. Figure 6 shows the resulting stellar background fit to cloud 2.

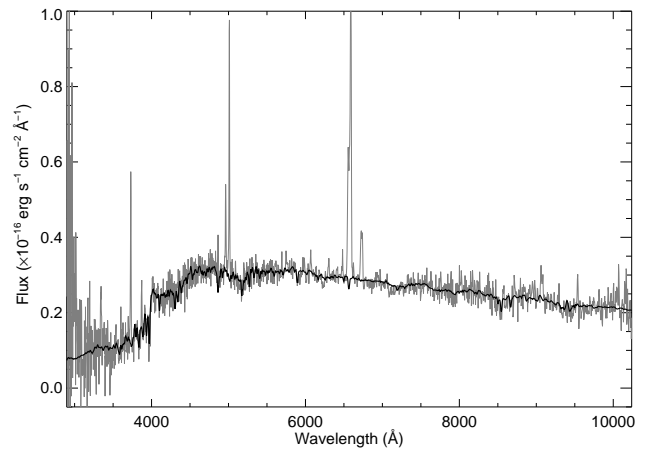


FIG. 6.— Observed cloud 2 spectrum overplotted with the stellar population fit (thick black line) used to subtract the underlying stellar continuum.

Because we do not observe absorption features in the spectra of clouds 1 and 9 ( $r \gtrsim 2''$ ), we fit the stellar background of these clouds with a cubic spline. The background fit to cloud 1 is shown in Figure 7.

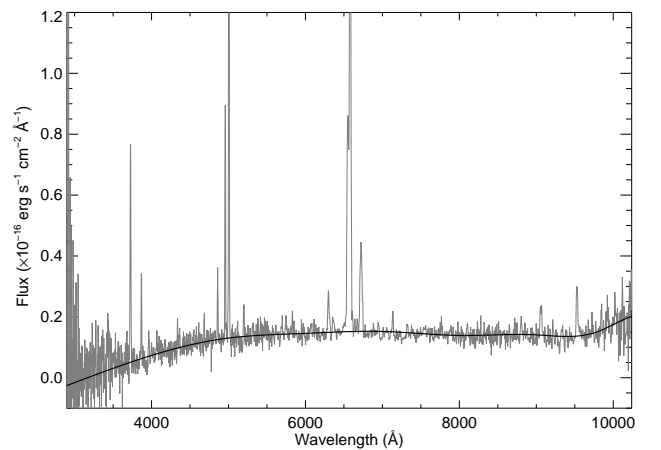


FIG. 7.— Observed cloud 1 spectrum overplotted with the cubic spline fit (thick black line) used to subtract the background continuum.

### 2.3. NLR Cloud Velocities

Cloud velocities and velocity dispersions were measured using the bright and unblended [O III]  $\lambda 5007$  line on the STIS G430M spectral image. The central wavelength and FWHM

TABLE 2. CLOUD VELOCITIES AND VELOCITY DISPERSIONS

Cloud	Radial Velocity (km s <sup>-1</sup> )	Velocity Dispersion (km s <sup>-1</sup> )
1	-145 (1)	107 (3)
2	85 (6)	202 (18)
3	116 (1)	25 (9)
3a	217 (6)	138 (13)
4	-37 (7)	66 (11)
4a	41 (7)	66 (10)
4b	-31 (4)	331 (13)
5	9 (1)	37 (2)
5a	-15 (2)	139 (5)
5b	45 (5)	338 (11)
6	30 (1)	22 (3)
6a	24 (4)	221 (13)
7	67 (2)	105 (6)
8	53 (7)	69 (11)
8a	-18 (9)	49 (15)
9	34 (1)	74 (3)

of each [OIII] $\lambda 5007$  line was obtained by fitting a single Gaussian plus a linear background to the spectral region adjacent to the line. Five clouds were not well fit by a single Gaussian in the higher spectral resolution G430M data, most likely due to a superposition of clouds along the line-of-sight. These clouds were fit using multiple Gaussian components. We label the additional clouds by appending the lower-case letters “a” and “b” to the cloud identifications (see Fig. 3).

Several of the emission-line clouds were not centered within the STIS slit. We determined the relative position of the clouds within the slit by using the *HST*/WFPC2 F502N narrowband image of the near-nuclear region of M51. We rotated the WFPC2 F502N image to the same position angle as our STIS observations (166°) and identified the emission-line clouds present our STIS spectra. Gaussian profiles were then fit to the NLR clouds in the F502N image to determine the difference between the cloud centroid and the center of the slit. These pixel differences were converted to velocity shifts and were used to correct the cloud radial velocities. At a given position along the slit multiple clouds are not spatially resolved in the WFPC2 images. Thus, the same slit offset correction was applied to clouds with multiple components.

The intrinsic velocity dispersion of each cloud was calculated by subtracting, in quadrature, the instrumental line broadening of 62 km s<sup>-1</sup> from the measured FWHM velocity widths of the [OIII] $\lambda 5007$  emission lines in the G430M spectral image. We used the *HST*/WFPC2 F502N image to estimate the instrumental broadening for clouds 2, 3, 5, and 6, which do not fully illuminate the slit width. The instrumental broadening for these clouds was found to be  $\sim 45$  km s<sup>-1</sup>.

The G430M [OIII] $\lambda 5007$  cloud velocities and velocity dispersions are presented in Table 2. The uncertainties were propagated from the errors in the Gaussian fits and are given in parenthesis. A systemic velocity of 463 km s<sup>-1</sup> (de Vaucouleurs et al. 1991) was subtracted from the radial velocities to correct for the recessional motion of the M51 host galaxy.

#### 2.4. Emission-Line Flux Measurements

The emission-line fluxes were measured using the IRAF routine SPECFIT. Isolated emission lines were measured using a Gaussian profile with a linear background. Since we detected weak residual, broad TiO absorption in the spectral region near the [O I] $\lambda\lambda 6300,6364$  lines, a quadratic background

was fit to the local continuum near these lines and subtracted prior to fitting the emission. The [ArIII] $\lambda 7136$  flux was measured by simple numerical integration across the line profile due to the weakness of this emission line and uncertainties in the TiO stellar absorption. The G430L [OIII] $\lambda 5007$  profile was used as a template to deblend the [NII] + H $\alpha$  lines and the [SII] $\lambda\lambda 6716,6731$  doublet in the G750L spectral images. Because the G430L and G750L grating modes have different spectral resolutions, the width of the G430L [OIII] profile was allowed to vary in the fits. Using the [OIII] profile to fit the H $\alpha$  line allowed for one less free parameter and resulted in more reliable fits to the blended [NII] + H $\alpha$  complex. For cases in which both the Gaussian and [OIII] template fit gave reliable results, the H $\alpha$  fluxes agreed within 2%. The [NII] $\lambda\lambda 6548,6583$  doublet lines were constrained to have the same FWHM velocity widths, fixed relative central wavelengths, and an intensity ratio fixed by atomic physics (1.295). The H $\alpha$  FWHM was fixed to the value of the [NII] $\lambda\lambda 6548,6583$  lines. Similarly, the [SII] $\lambda\lambda 6716,6731$  doublet lines were constrained to have fixed relative central wavelengths and identical FWHM velocity widths.

#### 2.5. Reddening Correction

We used the observed Balmer decrement of the H $\alpha$ /H $\beta$  line ratio to estimate the reddening of each NLR cloud. The reddening curve of Fitzpatrick (1999) was applied assuming an intrinsic H $\alpha$ /H $\beta$  ratio of 3.1. While case B recombination yields H $\alpha$ /H $\beta$ =2.85 for  $n_e = 10^4$  cm<sup>-3</sup> and  $T_e = 10^4$  K (Brocklehurst 1971), an assumed ratio of H $\alpha$ /H $\beta$ =3.1 is more appropriate due to collisional excitation of H $\alpha$  in AGN environments (Ho et al. 1993, and references therein). The largest values of  $E(B-V)$  ( $\sim 0.37$ ,  $A_V = 1.1$  mag) are found for the two innermost NLR clouds (4 and 5), which straddle the central dust lane.

To account for the differential reddening across clouds 4 and 5, each cloudlet spectrum was separately dereddened before summing the cloud flux. The values of  $E(B-V)$  and the dereddened emission-line fluxes, normalized to H $\beta$ , are presented in Table 3. The propagated dereddened flux errors are given in parentheses.

### 3. RESULTS

#### 3.1. NLR Morphology

The continuum-subtracted *HST*/WFPC2 narrowband [OIII] (Fig. 8a) and [NII] + H $\alpha$  images (Fig. 8b) of the near-nuclear region of M51 suggest the presence of a biconical morphology for the inner NLR gas. In the AGN paradigm, ionization cones result from the collimation of the nuclear continuum radiation field by a dense, optically-thick molecular torus and have been previously observed in several Seyfert galaxies (Pogge 1988; Evans et al. 1993; Wilson & Tsvetanov 1994). Most of the emission in the near-nuclear region of M51 appears confined to an ionization cone with a projected opening angle of  $\sim 74^\circ$  with an axis position angle of  $\sim 163^\circ$  (see Figures 8a and 8b).

On the southern side of the nucleus, the [NII] + H $\alpha$  image (Fig. 8b) shows a shell-like structure whose boundary agrees well with the boundaries defined by the inner ionization cone. The eastern shell boundary is more prominent and better defined than the western side, which appears to be fragmented. Inside of the shell-like structure, we find a hollow cavity that is occupied by the southern radio jet. The most probable origin of the cavity is that it has been evacuated by the radio jet (see § 4). Thus, the edges of the southern cone structure

TABLE 3. DEREDDENED EMISSION-LINE FLUXES (NORMALIZED TO H $\beta$ )

Line	Cloud 1	Cloud 2	Cloud 3	Cloud 4	Cloud 5	Cloud 6	Cloud 7	Cloud 8	Cloud 9
[Ne V] $\lambda$ 3346	...	...	...	0.18 (0.04)	0.23 (0.05)	...	...	...	...
[Ne V] $\lambda$ 3426	...	...	...	0.40 (0.10)	0.98 (0.14)	...	...	...	...
[O II] $\lambda\lambda$ 3727	4.39 (2.85)	5.57 (4.27)	3.24 (1.65)	1.91 (0.33)	1.23 (0.15)	1.26 (0.28)	1.93 (0.96)	2.63 (1.16)	1.92 (1.29)
[Ne III] $\lambda$ 3869	1.46 (0.93)	1.35 (1.04)	0.83 (0.48)	0.99 (0.17)	1.10 (0.14)	0.62 (0.15)	...	0.97 (0.43)	0.43 (0.33)
[Ne III] $\lambda$ 3968	0.44 (0.27)	0.40 (0.29)	...	0.29 (0.05)	0.32 (0.04)	0.18 (0.04)	...	0.29 (0.12)	...
H $\delta$ $\lambda$ 4102	0.18 (0.13)	...	...	0.23 (0.06)	0.31 (0.05)	0.26 (0.07)	...	...	...
H $\gamma$ $\lambda$ 4340	0.45 (0.28)	0.70 (0.54)	...	0.59 (0.10)	0.43 (0.06)	0.42 (0.10)	0.49 (0.26)	0.27 (0.14)	...
[O III] $\lambda$ 4363	0.50 (0.32)	...	...	...	...	...	...	...	...
He II $\lambda$ 4686	0.41 (0.25)	...	0.33 (0.19)	0.25 (0.04)	0.32 (0.04)	0.23 (0.06)	0.34 (0.17)	0.34 (0.14)	0.32 (0.21)
H $\beta$ $\lambda$ 4861	1.00 (0.57)	1.00 (0.68)	1.00 (0.45)	1.00 (0.14)	1.00 (0.10)	1.00 (0.19)	1.00 (0.43)	1.00 (0.39)	1.00 (0.58)
[O III] $\lambda$ 4959	3.92 (2.18)	1.74 (1.14)	2.44 (1.05)	2.77 (0.38)	3.80 (0.36)	1.78 (0.33)	1.02 (0.43)	2.13 (0.80)	1.77 (1.00)
[O III] $\lambda$ 5007	11.27 (6.23)	4.96 (3.24)	6.92 (2.97)	7.87 (1.08)	10.76 (1.02)	5.11 (0.94)	2.94 (1.23)	6.11 (2.29)	5.10 (2.87)
[N I] $\lambda\lambda$ 5200	0.80 (0.44)	0.48 (0.32)	0.32 (0.15)	0.43 (0.06)	0.26 (0.03)	0.31 (0.07)	0.44 (0.20)	0.58 (0.22)	0.25 (0.15)
[O I] $\lambda$ 6300	1.49 (0.73)	0.66 (0.40)	0.52 (0.21)	0.59 (0.08)	0.35 (0.04)	0.43 (0.09)	0.64 (0.27)	0.61 (0.21)	1.10 (0.56)
[O I] $\lambda$ 6364	0.48 (0.23)	...	...	0.18 (0.02)	0.11 (0.01)	0.14 (0.02)	...	0.19 (0.06)	...
[N II] $\lambda$ 6548	4.79 (2.29)	2.89 (1.64)	2.18 (0.81)	3.15 (0.37)	2.20 (0.18)	2.32 (0.37)	2.53 (0.92)	3.10 (1.01)	2.82 (1.37)
H $\alpha$ $\lambda$ 6563	3.09 (1.51)	3.07 (1.76)	3.06 (1.15)	3.06 (0.37)	3.06 (0.25)	3.09 (0.50)	2.88 (1.05)	3.09 (1.02)	3.09 (1.54)
[N II] $\lambda$ 6583	14.33 (6.85)	8.30 (4.70)	6.32 (2.36)	9.27 (1.10)	6.53 (0.54)	6.88 (1.11)	7.55 (2.74)	9.09 (2.96)	8.21 (4.02)
[S II] $\lambda$ 6716	1.90 (0.92)	1.19 (0.68)	0.88 (0.33)	0.99 (0.12)	0.88 (0.08)	1.06 (0.19)	1.08 (0.43)	1.13 (0.39)	1.31 (0.70)
[S II] $\lambda$ 6731	1.71 (0.84)	1.14 (0.65)	0.90 (0.34)	1.06 (0.13)	0.88 (0.08)	1.15 (0.21)	1.26 (0.48)	1.34 (0.44)	1.34 (0.68)
[Ar III] $\lambda$ 7136	0.49 (0.24)	...	0.23 (0.10)	0.19 (0.03)	0.25 (0.02)	0.22 (0.06)	...	0.43 (0.15)	0.32 (0.19)
[S III] $\lambda$ 9069	0.96 (0.44)	...	...	0.54 (0.06)	0.65 (0.06)	0.72 (0.12)	0.68 (0.31)	0.63 (0.21)	0.53 (0.25)
[S III] $\lambda$ 9532	1.47 (0.64)	0.95 (0.51)	0.88 (0.30)	1.14 (0.12)	1.22 (0.09)	1.26 (0.19)	1.29 (0.47)	1.41 (0.42)	0.73 (0.34)
F(H $\beta$ ) <sup>a</sup>	3.16 (1.27)	3.54 (1.70)	7.66 (2.43)	36.83 (3.70)	35.73 (2.46)	11.62 (1.57)	2.32 (0.71)	4.43 (1.21)	2.03 (0.83)
E(B-V)	0.09 (0.12)	0.32 (0.14)	0.40 (0.09)	0.35 (0.03)	0.38 (0.02)	0.11 (0.04)	0.00 (0.09)	0.15 (0.08)	0.10 (0.12)

NOTE. — Fluxes are relative to H $\beta$ . Errors are given in parenthesis.<sup>a</sup>Dereddened H $\beta$  Flux ( $\times 10^{-16}$  erg s $^{-1}$  cm $^{-2}$ ).

may be dominated by shocks expanding laterally from the radio jet instead of photoionization from the nuclear continuum source. While our single slit position does not intersect these boundaries, *HST* GO program 9147 (Ferruit et al., in preparation) will map the emission near the radio jet to determine the source of ionization in these structures.

Additionally, the overall position angle of the optical emission is closely aligned with the observed radio emission at 3.6 cm and 6 cm (Crane & van der Hulst 1992). Recent CO imaging of M51 (Scoville et al. 1998) has revealed dense molecular gas confined to a disk that is associated with the more opaque arm of the X-shaped dust absorption feature that crosses the nucleus. This molecular gas is nearly perpendicular to the radio jet (Ford et al. 1996; Grillmair et al. 1997) and has a density  $\geq 10^5 \text{ cm}^{-3}$ , which is sufficient to collimate both the ionizing continuum and the radio-emitting plasma (Scoville et al. 1998). This putative molecular torus may also provide a reservoir of matter to feed the active nucleus.

Extensive kinematic modelling by Cecil (1988) indicates that the jet axis is oriented  $\sim 70^\circ$  with our line-of-sight. If the radio jet and optical bicone axis are similarly collimated and nearly co-spatial, then the resulting inclination angle for the ionization cone is  $\sim 20^\circ$ , with the southern cone being nearer.

### 3.2. Kinematics

We plot the cloud radial velocities and velocity dispersions as a function of projected radial distance from the nucleus in Figure 9. The amplitude of the NLR cloud radial velocities are relatively small and lie in the range from  $-145 \text{ km s}^{-1}$  (cloud 1) to  $217 \text{ km s}^{-1}$  (cloud 3a). We find the smallest radial velocities ( $|v| \leq 67 \text{ km s}^{-1}$ ) for the nine clouds north of the nucleus (clouds 5–9). Only five of the NLR clouds (1, 4, 4b, 5a, and 8a) have blueshifted radial velocities, while the remaining 11 clouds are redshifted. The highest velocity dispersions ( $\Delta v \approx 340 \text{ km s}^{-1}$ ) are found closest to the nucleus (clouds 4b and 5b), and the upper-envelope of velocity dispersions decreases as the projected radial distance increases.

In Figure 9 we have overplotted a simple inclined Keplerian disk model by assuming the NLR clouds lie in the plane of the M51 host galaxy (inclination=20°, eastern side nearer, with major axis along P.A.=170°, Tully 1974) and are undergoing gravitational rotation about a central mass of  $1 \times 10^8 M_\odot$ . It is evident that both qualitatively and quantitatively this model does not fit the observed radial velocity field of the NLR clouds. Most of the clouds north of the nucleus are redshifted, however, we would expect them to exhibit blueshifted radial velocities if they were located within the galactic disk. The lack of any obvious S-shape in the radial velocity distribution suggests that the NLR clouds are not undergoing gravitational rotation in a circumnuclear disk.

An alternative explanation for the kinematic structure is that the NLR clouds are outflowing (or inflowing) from the nucleus. Radial outflow motions have been observed in several studies of the NLR in Seyfert galaxies (e.g. Kaiser et al. 2000; Crenshaw & Kraemer 2000; Ruiz et al. 2001). The relatively small observed radial velocities on the northern side of the nucleus are consistent with an outflow (or inflow) that lies nearly in the plane of the sky. This picture is consistent with the clouds lying near the front half of the ionization cone (see Figures 8a and 8b), which we have also inferred to lie nearly in the plane of the sky. While our kinematic data cannot conclusively discriminate between outflow and inflow radial motions, the presence of the southern radio jet and a possible northern counter-jet favor the outflow scenario.

Clouds 1, 3, and 3a, located on the southern side of the nucleus, possess the largest observed radial velocities ( $|v| \geq 116 \text{ km s}^{-1}$ ). Interestingly, these clouds lie on the same side of the nucleus as the radio jet and have nearly coincident radio knots (see § 4). While cloud 1 is consistent with entrainment by the jet outflow, clouds 2, 3, and 3a are not. For a jet orientation of 70° with the line-of-sight (Cecil 1988), these clouds should exhibit blueshifted radial velocities if they are entrained by the jet. A possible explanation for the larger radial velocities of these clouds is that they lie behind the radio jet and have offset velocities due to a laterally expanding flow away from the radio jet. If there was a weak northern counter jet, which has since disrupted, we would expect clouds north of the nucleus to be redshifted and those south of the nucleus to be blueshifted. We see a very weak signature supporting this scenario in both our kinematic and radio observations.

Assuming that cloud 1 is entrained by the jet outflow (70° to the line-of-sight), the resulting deprojected velocity of this cloud is  $424 \text{ km s}^{-1}$ . This velocity is in agreement with the previously inferred shock velocity of  $\sim 500 \text{ km s}^{-1}$  (Cecil 1988) and is roughly consistent with the  $690 \text{ km s}^{-1}$  shock velocity inferred from the *Chandra* X-ray temperature (Terashima & Wilson 2001).

Cloud 1 lies at the northern edge of the XNC near the location where the radio jet impinges on the radio lobe. Cecil (1988) decomposed the XNC into several kinematic components using ground-based ( $\sim 1''$  resolution) Fabry-Perot observations at  $65 \text{ km s}^{-1}$  resolution, which is similar to our  $62 \text{ km s}^{-1}$  resolution at  $[\text{O III}]\lambda\lambda 5007$  in G430M. We note that his blueshifted XNC component ( $v = -180 \text{ km s}^{-1}$ ,  $\Delta v = 140 \text{ km s}^{-1}$ ) is in close agreement with our measurements for cloud 1 ( $v = -145 \text{ km s}^{-1}$ ,  $\Delta v = 104 \text{ km s}^{-1}$ ).

### 3.3. Spectral Classification

Based upon optical studies of the emission-line ratios, M51 has been previously classified as a LINER (e.g. Stauffer 1982; Filippenko & Sargent 1985; Carrillo et al. 1999), a Seyfert/LINER transition object (Heckman 1980), and a Seyfert 2 (e.g. Ho et al. 1997). Our NLR cloud spectra exhibit strong emission lines of  $[\text{O III}]\lambda\lambda 4959, 5007$ ,  $[\text{N II}]\lambda\lambda 6548, 6583$ ,  $[\text{O II}]\lambda\lambda 3727$ , and  $[\text{S II}]\lambda\lambda 6716, 6731$  that are typical in Seyfert 2 spectra.

To classify emission-line objects, Baldwin, Phillips, & Terlevich (1981) used a series of two-dimensional emission-line ratio diagnostic plots to discriminate among various ionization mechanisms. We adopted this methodology and followed the convention of Veilleux & Osterbrock (1987, hereafter VO) who chose ratios of bright emission lines that are close together in wavelength to minimize the impact of dereddening errors. Figures 10, 11, and 12 show the three VO diagrams of  $[\text{O III}]\lambda 5007/\text{H}\beta$  versus  $[\text{N II}]\lambda 6583/\text{H}\alpha$ ,  $[\text{S II}]\lambda\lambda 6716, 6731/\text{H}\alpha$ , and  $[\text{O I}]\lambda 6300/\text{H}\alpha$ , respectively.

Because the partially-ionized transition zone in nebula photoionized by young, hot stars is limited in size (Strömgren 1939), HII regions and starburst galaxies typically exhibit weaker ionization lines than those observed in LINERs or Seyferts. While both LINERs and Seyferts are ionized by more energetic sources, LINERs are distinguished from Seyferts by their lower excitation, which is indicated in part by a lower value of  $[\text{O III}]\lambda 5007/\text{H}\beta$  (Ho et al. 1993).

In Figures 10, 11, and 12 we denote the loci of points typically occupied by HII regions, LINERs, and Seyferts. To represent the regions photoionized by OB stars, which

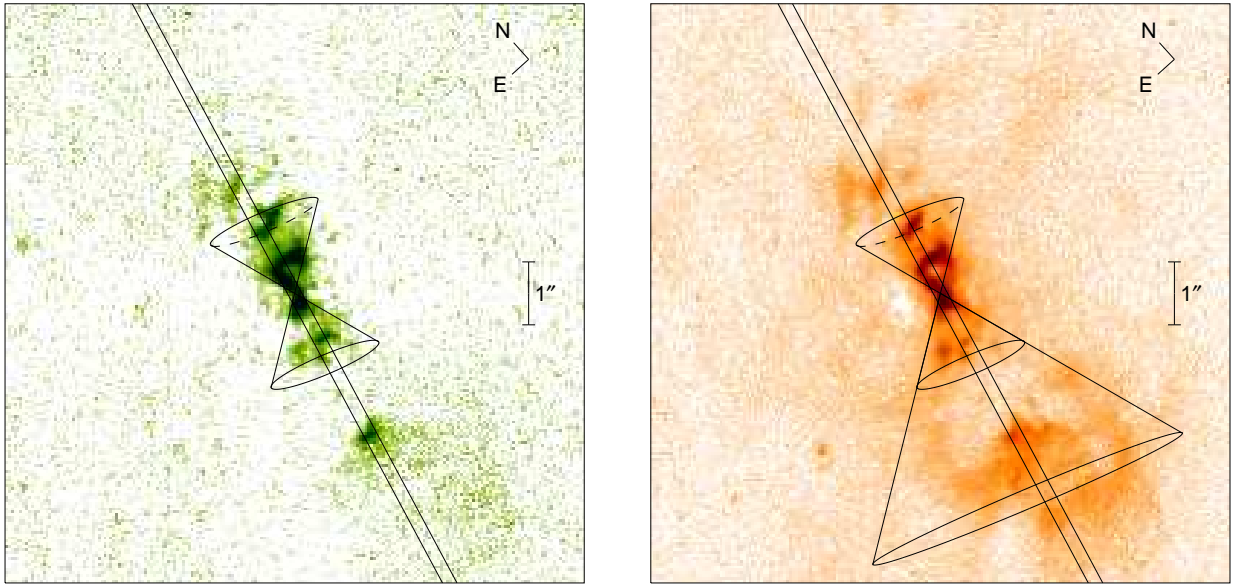


FIG. 8.— (a) Continuum-subtracted *HST*/WFPC2 F502N narrowband [OIII] image and (b) *HST*/WFPC2 F656N narrowband [NII] + H $\alpha$  image showing the biconical emission. The overplotted bicone has a projected opening angle of 74° with an axis position angle of 163°. The location of the 52''  $\times$  0.2'' slit for our STIS observations (P.A.=166°) also is shown.

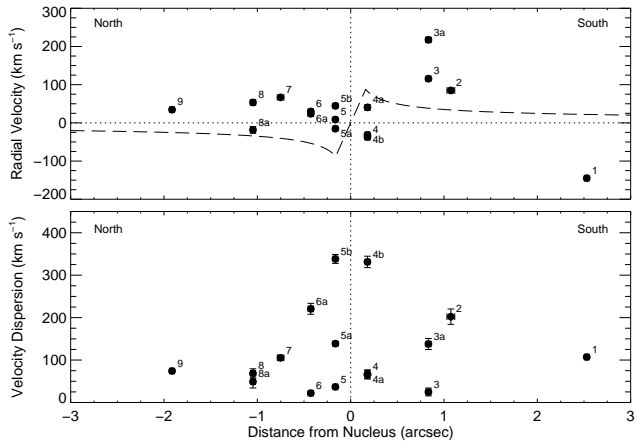


FIG. 9.— Radial velocities (upper panel) and velocity dispersions (lower panel) of the NLR clouds as a function of projected radial distance from the nucleus. The data points are labeled with the cloud identifications. The dashed line represents a simple inclined Keplerian disk model in which the clouds are assumed to lie in the plane of the galaxy ( $i = 20^\circ$ ) and are undergoing gravitational rotation about a central mass of  $1 \times 10^8 M_\odot$ . This model clearly does not fit the observed NLR kinematics.

include HII regions and starburst galaxies, we plotted the theoretical HII model sequence of McCall et al. (1985) for  $T_* = 38,500 - 47,000$  K. The M51 emission-line ratios occupy regions consistent with Seyfert galaxies. In general we find higher excitation, as measured by the [OIII]/H $\beta$  line ratios, for the NLR clouds than is typically observed in LINER galaxies. Cloud 7, our weakest NLR cloud, has a somewhat lower value of [OIII]/H $\beta$ , but it lies near the Seyfert/LINER boundary.

Figure 10 indicates that M51 possesses larger [NII] $\lambda 6583/\text{H}\alpha$  ratios ( $\simeq 2.7$ ) than the region typically occupied by Seyfert nuclei. We believe this to be an abundance effect, whereby nitrogen is selectively enhanced in the

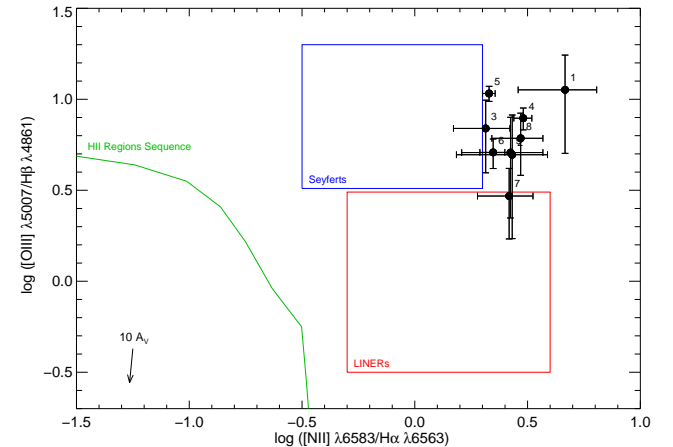


FIG. 10.— [OIII] $\lambda 5007/\text{H}\beta$  vs. [NII] $\lambda 6583/\text{H}\alpha$  diagnostic plot for the emission-line clouds. The loci of points typically occupied by Seyferts and LINERs are denoted by the colored boxes. The green line represents the theoretical HII region track of McCall et al. (1985). The arrow indicates the direction of the reddening correction.

near-nuclear region of M51 by factors of  $\sim 3 - 4.5$  (see § 5.2).

#### 3.4. Ionization State of the Gas

The ionization state of the NLR gas can be examined through the use of the [OIII] $\lambda 5007/\text{H}\beta$  ratio and the abundance insensitive [OIII] $\lambda 5007/[O\text{II}]\lambda\lambda 3727$  and [OIII] $\lambda 5007/[O\text{I}]\lambda 6300$  line ratios. The [OIII] $\lambda 5007/[O\text{II}]\lambda\lambda 3727$  line ratio is roughly proportional to the ionization parameter for radiation-bounded clouds and is relatively independent of the shape of the ionizing continuum (Penston et al. 1990).

Figures 13a–c show [OIII] $\lambda 5007/\text{H}\beta$ , [OIII] $\lambda 5007/[O\text{II}]\lambda\lambda 3727$ , and [OIII] $\lambda 5007/[O\text{I}]\lambda 6300$ , respectively, as a function of projected radial distance from the nucleus. In general, these line ratios are larger near

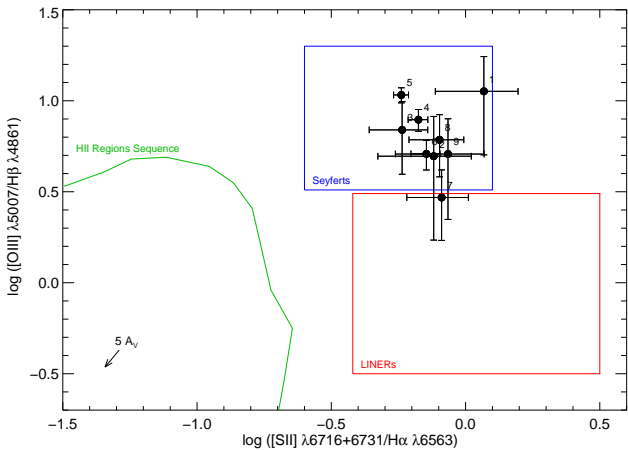


FIG. 11.— As in Fig. 10, but for  $[\text{OIII}] \lambda 5007/\text{H}\beta$  vs.  $[\text{SII}] \lambda \lambda 6716, 6731/\text{H}\alpha$ .

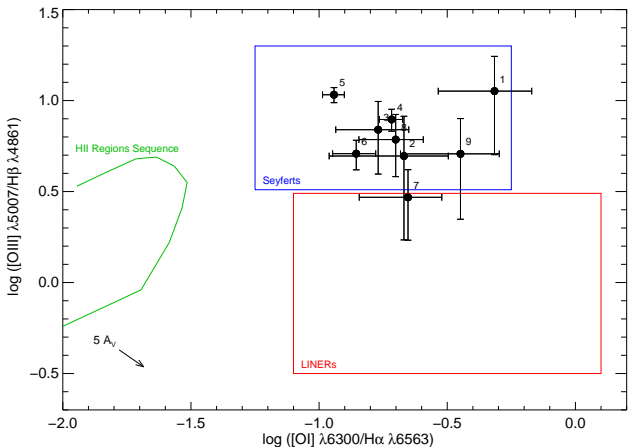


FIG. 12.— As in Fig. 10, but for  $[\text{OIII}] \lambda 5007/\text{H}\beta$  vs.  $[\text{OI}] \lambda 6300/\text{H}\alpha$ .

the nucleus and decrease with increasing radius out to  $\sim 1''$ . As a comparison, we have also overplotted three  $r^{-n}$  ( $n = 0.5, 0.6, 1.0$ ) curves, which qualitatively agree with the data, on Figures 13a–c. The declining line ratios indicate that the excitation of the NLR gas decreases with increasing radius within the near-nuclear region. As an exception, cloud 1 possesses the largest value of  $[\text{OIII}] \lambda 5007/\text{H}\beta$  (even larger than the innermost clouds 4 and 5), which may indicate the presence of an additional source of ionization (e.g. shocks) in this cloud.

### 3.5. Electron Density

In the low-density regime, the  $[\text{SII}] \lambda \lambda 6716, 6731$  doublet is a well-known electron density diagnostic that is relatively insensitive to temperature (Osterbrock 1989). This diagnostic can be applied in regions where the electron density is less than the critical density of  $[\text{SII}]$  ( $3.3 \times 10^3 \text{ cm}^{-3}$ ). Above this density the lines become collisionally de-excited. Unfortunately, the  $[\text{SII}] \lambda \lambda 6716, 6731$  lines are severely blended in our data. The wavelength separation of these lines (14.4 Å) is less than the spectral resolution of the G750L grating mode (18.3 Å). We deblended the  $[\text{SII}] \lambda \lambda 6716, 6731$  doublet using the  $[\text{OIII}] \lambda 5007$  line as a template, however, the result-

ing flux errors are large (Fig. 13d). We note that for a  $[\text{SII}] \lambda 6716/\lambda 6731$  ratio near unity, a 10% error in each of the emission lines results in nearly a factor of two uncertainty in the electron density.

To calculate the electron density of each NLR cloud (Table 4), we used the “temden” routine of the IRAF NEBULAR package, which uses a five-level atom approximation (Shaw & Dufour 1995). For clouds 2–9, we assumed an electron temperature  $T_e = 10^4 \text{ K}$ , which is typical for photoionized gas in the NLR of Seyfert galaxies. For cloud 1, we used an electron temperature of  $2.4 \times 10^4 \text{ K}$ , which was calculated from the observed  $[\text{OIII}]$  emission lines (see § 3.6). The resulting electron densities lie in the range between  $490 \text{ cm}^{-3}$  and  $1150 \text{ cm}^{-3}$ , however, no trend in the gas density as a function of radius can be inferred given the large flux errors. The average  $[\text{SII}]$  electron density within the NLR gas is  $770 \text{ cm}^{-3}$ . Cloud 1, located at the largest radial distance ( $2''$ ), possesses the lowest electron density of  $n_e = 490 \text{ cm}^{-3}$ .

We compare our results with those of Rose & Searle (1982) who adopted an average value of  $[\text{SII}] \lambda 6716/\lambda 6731 = 1.0$  for the entire nuclear region of M51 ( $61.''4 \times 2''$  slit). These authors assumed  $T_e = 8 \times 10^3 \text{ K}$  and calculated an electron density of  $630 \text{ cm}^{-3}$ . If we adopt this electron temperature, we find an average electron density of  $690 \text{ cm}^{-3}$ , which is in very good agreement with their value. Further, our results are similar to those of Rose & Cecil (1983) who found in a  $5''$  circular aperture an average  $[\text{SII}] \lambda 6716/\lambda 6731 = 0.93$ , corresponding to an electron density of  $880 \text{ cm}^{-3}$  for  $T_e = 7620 \text{ K}$ . Our calculated electron densities are also consistent with those found by Ford et al. (1985) who obtained electron densities in the range  $640$ – $720 \text{ cm}^{-3}$  for the nucleus of M51 and  $370$ – $490 \text{ cm}^{-3}$  for the XNC.

### 3.6. Electron Temperature

The electron temperature can be estimated from the observed  $[\text{OIII}] (\lambda 4959 + \lambda 5007)/\lambda 4363$  ratio. The difficulty in using this diagnostic is that the  $[\text{OIII}] \lambda 4363$  emission line generally is very weak in Seyfert spectra. For our NLR cloud spectra, we observed  $[\text{OIII}] \lambda 4363$  only in cloud 1. Using the NEBULAR package, we calculated an electron temperature of  $24,000 \text{ K}$  for this cloud (assuming an electron density of  $490 \text{ cm}^{-3}$ ). Electron temperatures of this scale typically are not observed in the  $\text{O}^{+2}$  zone of photoionized gas (Kraemer et al. 1998), providing further evidence that shocks contribute to the ionization structure of this cloud.

Because the  $[\text{OIII}] \lambda 4363$  line was too weak to be detected in the other NLR clouds, we derived upper limits for the electron temperature of the other clouds by numerically integrating the flux over the strongest noise feature in the spectrum near 4363 Å (Table 4). The resulting electron temperature is  $\lesssim 11,000 \text{ K}$  for the three innermost clouds (4–6) and cloud 8. These temperatures effectively rule out collisional ionization as the dominant source of excitation in these clouds as electron temperatures  $T_e < 20,000 \text{ K}$  are too low for this mechanism to be important (Wilson 1993).

Clouds 3 and 9 have electron temperatures  $T_e \lesssim 17,500 \text{ K}$ , which also suggests that the ionization of these clouds is primarily due to photoionization. The upper limits for the temperature of clouds 7 and 2 are  $19,000 \text{ K}$  and  $21,800 \text{ K}$ , respectively. It is most likely that these represent weak constraints and the large upper limits are due to the lower signal-to-noise of these clouds, which are fainter than the inner NLR clouds and cloud 1. While it remains that the larger upper-limit to the electron temperatures could possibly indicate a greater role

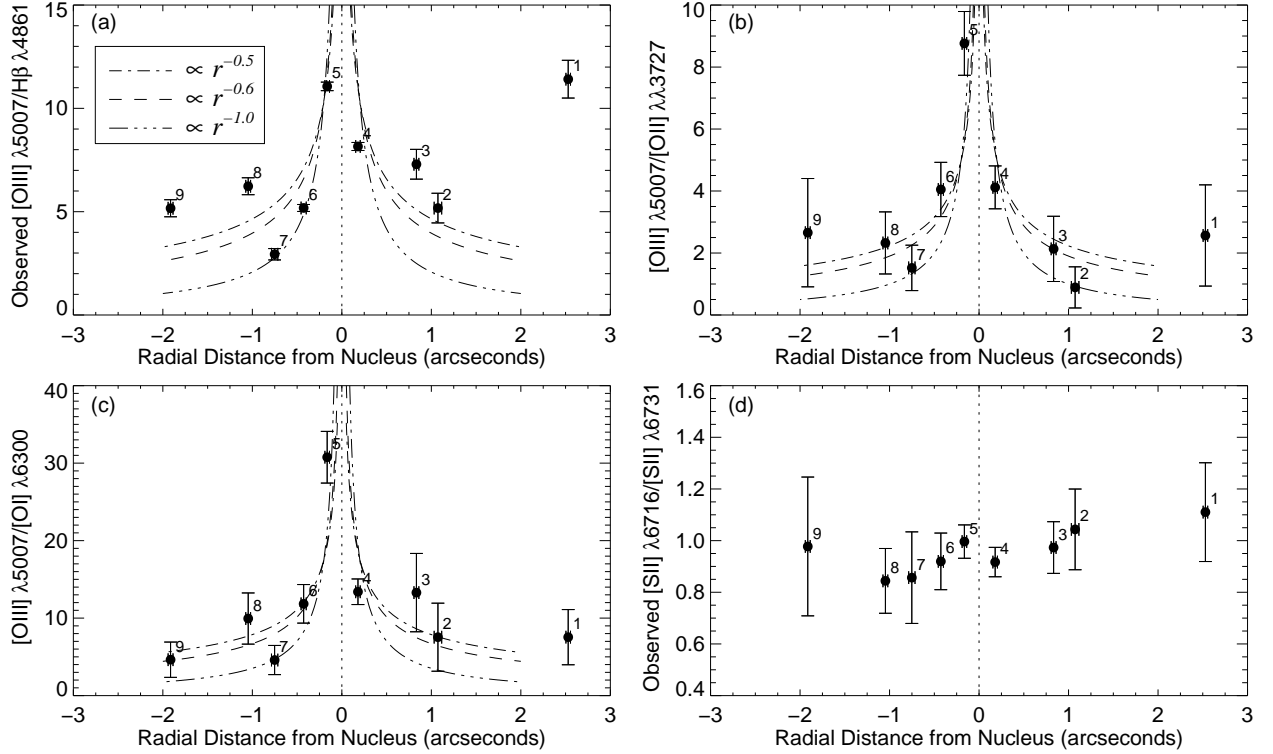


FIG. 13.— (a)  $[\text{OIII}] \lambda 5007/\text{H}\beta$  (b)  $[\text{OIII}] \lambda 5007/[\text{OII}] \lambda\lambda 3727$  (c)  $[\text{OIII}] \lambda 5007/[\text{OI}] \lambda 6300$  and (d)  $[\text{SII}] \lambda 6716/[\text{SII}] \lambda 6731$  for the nine NLR emission-line clouds plotted as a function of radial distance from the nucleus.

TABLE 4. PHYSICAL CONDITIONS IN THE NLR CLOUDS ALONG P.A.  $166^\circ$

Cloud	Radius <sup>a</sup> ('', pc)	$n_e$ ( $\text{cm}^{-3}$ )	$T_e$ (K)	$L(\text{H}\beta)$ ( $10^{36} \text{ erg s}^{-1}$ )	Ionized Mass ( $M_\odot$ )
1	2.53 (103)	490	24,000	2.7	50
2	1.07 (44)	510	< 21,800	3.0	60
3	0.83 (34)	680	< 17,500	6.5	90
4	0.18 (7)	850	< 10,200	31.1	350
5	-0.16 (7)	620	< 9,900	30.2	470
6	-0.43 (18)	840	< 11,000	9.8	110
7	-0.75 (31)	1090	< 19,200	2.0	20
8	-1.05 (43)	1150	< 11,100	3.7	30
9	-1.91 (78)	670	< 15,800	1.7	30
Total	...	...	...	90.7	1210

<sup>a</sup>Positive values denote clouds south of the nucleus. Negative values denote clouds north of the nucleus.

for shocks, the MAPPINGS II shock models (see § 6) provide a poorer fit to these clouds than our photoionization models.

### 3.7. Ionized Mass

The mass of ionized gas in each NLR cloud can be estimated from the observed electron density and luminosity of the  $\text{H}\beta$  recombination line. For a completely ionized gas with solar helium abundances, the total ionized mass is given as (Osterbrock 1989)

$$M = \frac{1.4 m_H L(\text{H}\beta)}{\alpha_{\text{H}\beta}^{\text{eff}} n_e h \nu_{\text{H}\beta}}, \quad (1)$$

where  $m_H$  is the mass of a hydrogen atom,  $L(\text{H}\beta)$  is the observed luminosity ( $\text{erg s}^{-1}$ ) of the  $\text{H}\beta$  recombination line,  $\alpha_{\text{H}\beta}^{\text{eff}}$  is the Case B effective  $\text{H}\beta$  recombination coefficient

( $3 \times 10^{-14} \text{ cm}^3 \text{ s}^{-1}$  at  $10^4 \text{ K}$ , Osterbrock 1989),  $n_e$  is the electron density, and  $h \nu_{\text{H}\beta}$  is the energy of an  $\text{H}\beta$  photon. We derived the  $\text{H}\beta$  luminosities by correcting the observed  $\text{H}\beta$  emission-line fluxes for the distance to M51 of 8.4 Mpc (Feldmeier et al. 1997). The electron densities were taken as those derived in § 3.5 for the [SII] emitting region. The resulting ionized masses of each NLR cloud are shown in Table 4. The total ionized mass of the NLR clouds in our  $52'' \times 0''.2$  slit is  $1.2 \times 10^3 M_\odot$ , with most of this mass located in the three innermost and brightest  $\text{H}\beta$  clouds. For comparison, Ford et al. (1985) derived a total ionized mass of  $4.4 \times 10^3 M_\odot$  within a larger  $2'' \times 2''$  region centered on the nucleus. While our slit position was chosen to intersect the bright [OIII] clouds straddling the nucleus and the bright NLR cloud located near the jet terminus, additional structures, such as two bright clouds north of nucleus and faint extended circumnuclear emission,

are included in Ford's measurement.

### 3.8. Ionizing Flux

The observed  $H\beta$  luminosity can also be used to calculate the total number of recombinations per second as (Peterson 1997)

$$Q(H) = \frac{L(H\beta)}{h\nu_{H\beta}} \frac{\alpha_B}{\alpha_{H\beta}^{eff}} = 2.11 \times 10^{12} L(H\beta) \text{ photons s}^{-1}, \quad (2)$$

where  $\alpha_B$  is the Case B hydrogen recombination coefficient ( $2.6 \times 10^{-13} \text{ cm}^3 \text{ s}^{-1}$  at  $10^4 \text{ K}$ , Osterbrock 1989).

For the nine NLR clouds located within our  $52'' \times 0.2''$  slit along position angle  $166^\circ$ , the total  $H\beta$  luminosity is  $9.1 \times 10^{37} \text{ erg s}^{-1}$  (see Table 4). Using the above equation, we derive a hydrogen recombination rate of  $Q(H) = 1.9 \times 10^{50} \text{ photons s}^{-1}$ . This number provides an estimate of the total number of hydrogen ionizing photons produced per second by the active nucleus by assuming ionization equilibrium, whereby the total number of hydrogen ionizing photons produced by the central source equals the total number of recombinations.

Because the observed  $H\beta$  luminosity was summed over our single slit position, we have not accounted for all of the NLR  $H\beta$  emission. As such,  $Q(H)$  represents a lower-limit to the rate of ionizing photons produced by the central source. Within a  $2'' \times 2''$  aperture, which as discussed previously contains emission structures not included in our narrow slit, Ford et al. (1985) reported a nuclear  $H\beta$  luminosity of  $2.8 \times 10^{38} \text{ erg s}^{-1}$ . This results in a total rate of hydrogen ionizing photons of  $5.9 \times 10^{50} \text{ photons s}^{-1}$ . These calculations show the relative weakness of the active nucleus of M51. For comparison, Schulz & Komossa (1993) derived a total rate of hydrogen ionizing photons of  $3 \times 10^{54} \text{ photons s}^{-1}$  for the central source of the luminous Seyfert 1 galaxy NGC 4151.

## 4. RADIO OBSERVATIONS

The existence of a radio jet and radio lobe on the southern side of the nucleus of M51 was first detected using VLA observations at 4.8 GHz (Crane & van der Hulst 1992). These authors found a sinuous radio jet, extending  $\sim 3''$ , that connected the weak nuclear radio source with a diffuse radio lobe, which has been identified with the optical XNC feature (Ford et al. 1985). The radio lobe was dominated by a bright arcuate, ridge-like structure extending approximately  $5''$ .

Our VLA-A 8.4 GHz observations (see Fig. 4) confirm the presence of the previously observed radio structures in the near-nuclear region of M51. The radio maps show a weak, unresolved radio core with a flux density of  $330 \mu\text{Jy}/\text{beam}$ . The southern radio jet spans  $2.3''$  (94 pc) and decreases in luminosity along its spatial extent, reaching a minimum of  $\sim 2-4 \mu\text{Jy}/\text{beam}$ . The position angle at the base of the jet is  $158^\circ$ . The radio jet terminates near a diffuse, extended lobe structure, however, it is not connected to the radio lobe at the lowest contour level. It appears that the radio jet connects to the southern radio lobe near the location of cloud 1, however, because of the low signal-to-noise of our radio observations we are unable to determine the precise location of the impingement. Although our resolution at 3.6 cm is better than the earlier 6 cm data (Crane & van der Hulst 1992), a comparison of the peak flux in the jet at these two wavelengths suggests that the spectral index is approximately 3.1. The total east-west extent of the southern radio lobe is  $5.3''$  (220 pc).

The nuclear source of M51 is also surrounded by a  $2''$  extended radio structure that is elongated along a position angle

of  $169^\circ$ . To the north-northwest of the nucleus, this structure turns into a ridge that extends approximately  $1.5''$  and could signify a bent northern counter-jet. Our 3.6 cm data do not exhibit the northern loop structure observed at 20 cm by Ford et al. (1985) and at 6 cm by Crane & van der Hulst (1992). Because this feature is only weakly detected at 6 cm, it is likely not present in our maps due to the lower signal-to-noise of our radio data and is probably not a result of the frequency difference.

In addition to the nuclear source structures, we find an elongated triple radio source at  $27.8''$  (1130 pc) north-northwest of the nucleus at a position angle of  $335^\circ$ . At the distance of M51, the spatial length of this structure is 86 parsec. The position angle of this northern source is within  $14^\circ$  of the position angle of the nuclear elongation, and it is possible that this triple structure is a remnant of past jet activity. However, it could also result from a weak radio galaxy in the background.

The centerline of the radio jet and its brightness distribution reveal a substantial non-linearity that is suggestive of bends and knots in the jet. We identify eleven radio knots along the entire north-south structure. The location and the flux density of these radio knots are presented in Table 5. The earlier 4.8 GHz radio maps only displayed two distinct hotspots.

Our VLA 8.4 GHz data reveal a slightly different jet orientation as compared to the earlier low-resolution 4.8 GHz data (Crane & van der Hulst 1992). Specifically, the position angle of the southern radio jet in our 8.4 GHz maps (observed in 1999) lies  $\sim 10^\circ$  to the east of the centerline of the earlier 4.8 GHz jet structure (observed in 1985/1986). Additionally, the brightness distribution of the jet and southern radio lobe structure appears different than the earlier observations. In particular, the southern lobe structure is rather patchy and does not exhibit the clear arcuate, emission-ridge structure that was observed in the earlier 4.8 GHz data.

A potentially intriguing explanation for the discrepancy in the radio structures in the south would be oscillatory structure in the jet. The total radio power in the nuclear region of M51 ( $2 \times 10^{19} \text{ W Hz}^{-1}$ ) is at the very bottom of the distribution of active galaxies (Condon 1992), and the relative weakness of the radio jet makes it susceptible to instabilities that can cause the jet to precess. Oscillatory structure may be the result of precession at the nucleus itself or from Kelvin-Helmholtz (KH) instabilities resulting from the velocity differences between the gas inside and outside the jet. The KH instability results in helical structure for the jet that shows an exponentially growing oscillation with distance along the jet. However, the deduced shift in position angle of a precessing jet is relatively large and would result in a precession period that is too short. The mis-orientation of the low- and high-resolution jets could be due to a limb-brightening effect, but this would require rather unrealistic frequency-dependent opacity variations across the width of the jet. Alternatively, the apparent shift could simply result from the signal-to-noise limitations of our data and the uniformly weighted map of Crane & van der Hulst (1992).

In Figures 14 and 15, we present the *HST*/WFPC2 [O III] and [N II] + H $\alpha$  narrowband images superposed with the VLA 8.4 GHz radio continuum contours. In order to align the radio core with the assumed location of the obscured nucleus, the radio image ( $0.29'' \times 0.26''$  resolution) was shifted relative to the optical images ( $0.09''$  resolution) by  $\Delta\alpha = 0.15''$  and  $\Delta\delta = -1.06''$ . The location of the nine optical emission-line clouds, the eleven radio knots, and the slit for the STIS spectra also have been indicated.

TABLE 5. RADIO-OPTICAL CORRELATIONS

Radio Cloud	Radius <sup>a</sup> ('', pc)	Radio Flux ( $\mu$ Jy/beam)	Optical Cloud	Radius <sup>a</sup> ('', pc)	$H\beta$ Flux ( $10^{-16}$ erg s $^{-1}$ cm $^{-2}$ )	Comments
North						
R10	-1.8 (73)	2.6	...	...	...	Adjacent to Cloud 9
R9	-1.2 (49)	2.2	Cloud 8	-1.05 (43)	4.43	Adjacent to Cloud 8
R8	-0.8 (33)	1.6	Cloud 7	-0.75 (31)	2.32	Adjacent to Cloud 8
R7	-0.6 (24)	2.8	Cloud 6	-0.43 (18)	11.62	Adjacent to Cloud 6
R6	-0.3 (12)	3.6	Cloud 5	-0.16 (7)	35.73	Adjacent to Clouds 5 & 6
Nucleus	0	155	...	0	...	
South						
R5	0.6 (24)	3.6	Cloud 3	0.83 (34)	7.66	Cloud 3 at edge of R5
R4	1.0 (41)	1.6	Cloud 2	1.07 (44)	3.54	See morphology note <sup>b</sup>
R3	1.4 (57)	2.6	...	...	...	See morphology note <sup>b</sup>
R2	1.7 (69)	2.6	...	...	...	See morphology note <sup>b</sup>
R1	2.3 (94)	3.1	Cloud 1	2.53 (103)	3.16	R0 & R1 straddle Cloud 1
R0	2.7 (110)	2.6	Cloud 1	2.53 (103)	3.16	R0 & R1 straddle Cloud 1

<sup>a</sup>Positive values denote clouds south of the nucleus. Negative values denote clouds north of the nucleus.

<sup>b</sup>Morphologically, the region between R4 and R1 appears as though it may have been evacuated by the radio jet.

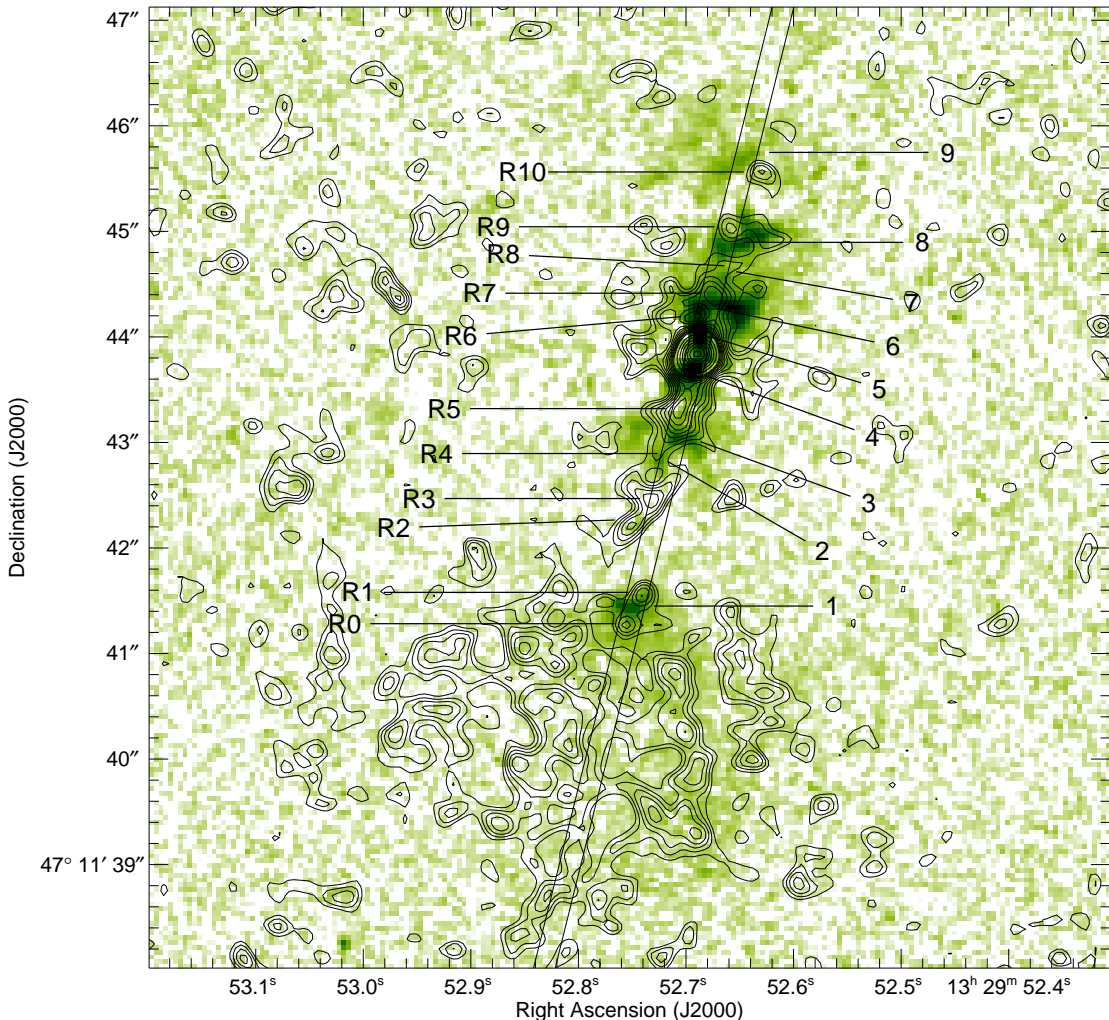


FIG. 14.—Continuum subtracted *HST*/WFPC2 F502N narrowband [OIII] image superimposed with our VLA 8.4 GHz radio contours. The contour levels are [2,3,4,5,6,7,8,9,10,11,12,16,20,24,28,32,36,40]  $\times$  5.0  $\mu$ Jy/beam. The location of the optical NLR clouds and radio knots have been indicated as well as the position of the STIS 52''  $\times$  0.5'' slit.

The radio structures are elongated with a position angle

close to that of the optical NLR emission observed in the *HST*

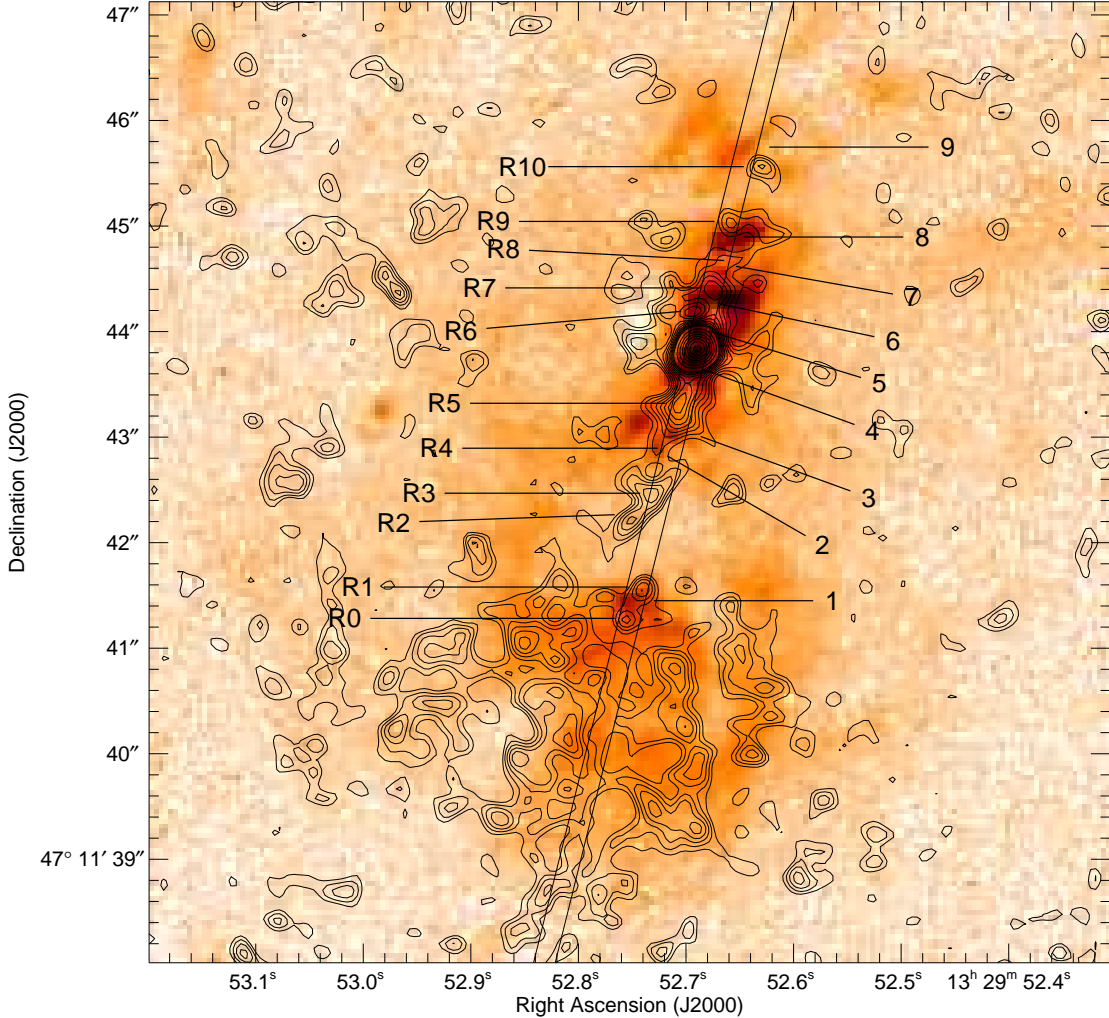


FIG. 15.— Continuum subtracted *HST*/WFPC2 F656N narrowband [N II] + H $\alpha$  image superimposed with our VLA 8.4 GHz radio contours. The contour levels are [2,3,4,5,6,7,8,9,10,11,12,16,20,24,28,32,36,40]  $\times$  5.0  $\mu$ Jy/beam. The location of the optical NLR clouds and radio knots have been indicated as well as the position of the STIS 52''  $\times$  0.2'' slit.

images. The STIS 52''  $\times$  0.2'' slit falls on most of the inner part of the elongated nuclear radio structure. Six of the nine optical NLR clouds located within our slit lie near the projected position of radio features. At the nucleus, the extended [N II] + H $\alpha$  and [O III] emission falls within the outer radio contours. The overall morphological agreement of the optical and radio emission at 8.4 GHz is very suggestive. We find that the optical emission-line clouds, in general, lie adjacent to the peaks of the radio emission. This spatial anti-coincidence suggests that the radio jet and its structural components do affect the optical emission regions and are associated as an energy source with the optical emission-line clouds. However, there are a couple of radio knots within the radio jet/optical bicone region that do not have nearby optical knots and thus, not all of the radio knots are anti-correlated with an emission-line cloud. While the radio resolution is  $\sim$  3 times worse than the optical image, it appears that the radio and optical knot anti-coincidence would still be present in a higher resolution radio map. South of the nucleus, it appears that the radio jet may have evacuated a conical region (see Fig. 15). In Table 5 we provide a more detailed comparison of the locations and

properties of the radio knots with the H $\beta$  emission from the optical clouds.

The [O III] and [N II] + H $\alpha$  *HST* images show that cloud 1, located 2.5'' south of the nucleus, falls within the radio lobe at the northern edge and coincides with a clear radio hotspot at location R0–R1. This hotspot could be interpreted as the entry point of the jet into the radio lobe. However, earlier observations by Cecil (1988) associate higher velocity dispersion gas east of this point with the entry point of the jet. Higher signal-to-noise radio observations are necessary to confirm the precise location at which the radio jet impinges the radio lobe.

The WFPC2 F656N [N II] + H $\alpha$  image shows an extended shell-like structure that surrounds the region where the radio jet is currently passing through. This shell is particularly prominent on the eastern side of the source, while it is fragmented on the western side. It is intriguing to interpret this shell structure as the boundary of a cavity region that has been evacuated by the radio jet. The excitation of this shell structure could be due to radiation emerging from the energy dissipation within the jet. Alternatively, the excitation of the shell could result from lateral expansion shocks generated by

the twisting jet.

## 5. PHOTOIONIZATION MODELS

We have generated photoionization models to determine if the NLR emission-line spectra are consistent with photoionization by a non-thermal central continuum source. The photoionization models were computed using version 94 of the photoionization code Cloudy (Ferland et al. 1998). The models were parameterized by the shape of the ionizing continuum, the dimensionless ionization parameter  $U$ , and the total hydrogen density  $n_H$ . The dimensionless ionization parameter  $U$  is defined as

$$U = \frac{1}{4\pi r^2 n_H c} \int_{\nu_0}^{\infty} \frac{L_{\nu}}{h\nu} d\nu, \quad (3)$$

where  $r$  is the distance from the inner (illuminated) face of the cloud to the central continuum source,  $n_H$  is the total hydrogen density,  $h\nu_0$  is the ionization energy of hydrogen (13.6 eV), and  $L_{\nu}$  is the frequency-dependent luminosity of the nuclear ionizing continuum. The models assume a constant density cloud with a plane-parallel geometry and emission-line photon escape from the illuminated face of the cloud.

### 5.1. Model Input Parameters

Photoionization models with solar abundances cannot reproduce the relatively strong observed  $[\text{N}\text{I}] \lambda\lambda 5200$  and  $[\text{N}\text{II}] \lambda\lambda 6548, 6583$  nitrogen lines in M51. We demonstrate this graphically in Fig. 16, where we have plotted the photoionization model grids for both solar and four times solar nitrogen ( $4 \text{ N}_{\odot}$ ). The best-fitting models require selective enhancement of nitrogen in the range of 3–4.5 times solar. The numerical abundances relative to hydrogen for a model with a factor of three overabundance of nitrogen are:  $\text{He} = 1.0 \times 10^{-1}$ ,  $\text{C} = 3.55 \times 10^{-4}$ ,  $\text{N} = 2.8 \times 10^{-4}$ ,  $\text{O} = 7.4 \times 10^{-4}$ ,  $\text{Ne} = 1.17 \times 10^{-4}$ ,  $\text{S} = 1.62 \times 10^{-5}$ , and  $\text{Ar} = 3.98 \times 10^{-6}$  (Grevesse & Anders 1989).

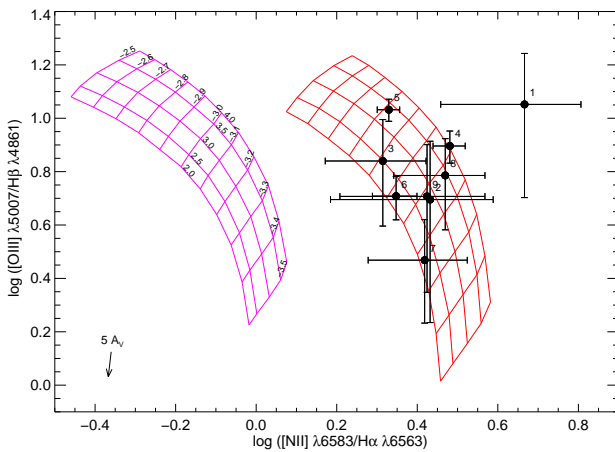


FIG. 16.—  $[\text{O}\text{III}] \lambda 5007/\text{H}\beta$  vs.  $[\text{N}\text{II}] \lambda 6583/\text{H}\alpha$  for the NLR clouds overplotted with our Cloudy photoionization model grids. The solar abundance model grid is shown in magenta and is labeled with  $\log U = -2.5$  to  $-3.5$  and  $\log n_H = 2$  to  $4 \text{ cm}^{-3}$ . The red grid shows the photoionization models with  $4 \times$  enhancement of the nitrogen abundance.

We also generated photoionization models that included the presence of dust grains within the line-emitting region. However, when compared to our observed optical emission lines,

these models are very similar to models without dust grains. Ultraviolet spectra and/or emission lines involving elements commonly found in dust grains can be useful for constraining models with dust. The IUE spectrum ( $10'' \times 20''$  elliptical aperture) of the nuclear region in M51 only shows the presence of a blended  $\text{Si}\text{III}] \lambda 1892$  and  $\text{C}\text{III}] \lambda 1909$  emission line attributed to HII regions (Ellis et al. 1982). We investigated whether the absence of  $\text{CIV} \lambda\lambda 1549$  from the IUE spectrum could be used to constrain dust models. For our highest excitation photoionization model, the  $\text{CIV} \lambda\lambda 1549$  reddening-corrected line flux ( $\sim 1 \times 10^{-15} \text{ erg s}^{-1} \text{ cm}^{-2}$ ) would be undetectable in the M51 IUE spectrum. Therefore without a more sensitive UV spectrum, we are unable to constrain models with dust grains. While the photoionization models that follow do not include the presence of dust grains within the NLR line-emitting region, we cannot rule out such models.

Using published M51 continuum flux measurements, we constructed a broadband spectral energy distribution (SED) to define the shape of the ionizing continuum. We assumed the SED was a power-law of the form  $F_{\nu} \propto \nu^{-\alpha}$ , where the spectral index,  $\alpha$ , was defined piecewise for different frequency intervals. Numerous photoionization models were generated to investigate the effect of changing the SED slope in all regions of the spectrum, in particular the UV to X-ray wavelength regime. As one would expect, the models were most sensitive to the spectral index in the extreme ultraviolet (EUV) region of the spectrum. We started with  $\alpha_{\text{EUV}} = 1.29$  ( $h\nu \gtrsim 13.6 \text{ eV}$ ), which was derived from the published data, and constructed several photoionization model grids by varying  $\alpha_{\text{EUV}}$  over the range 1–2. We found the best-fitting photoionization models occurred for  $\alpha_{\text{EUV}} = 1.35$ . In addition, we tested a model with the presence of an ultraviolet blue-bump in the ionizing continuum. However, this model produced a poorer fit to our observed line fluxes, especially for  $[\text{N}\text{I}] \lambda\lambda 5200$  and  $[\text{O}\text{I}] \lambda\lambda 6300, 6364$ .

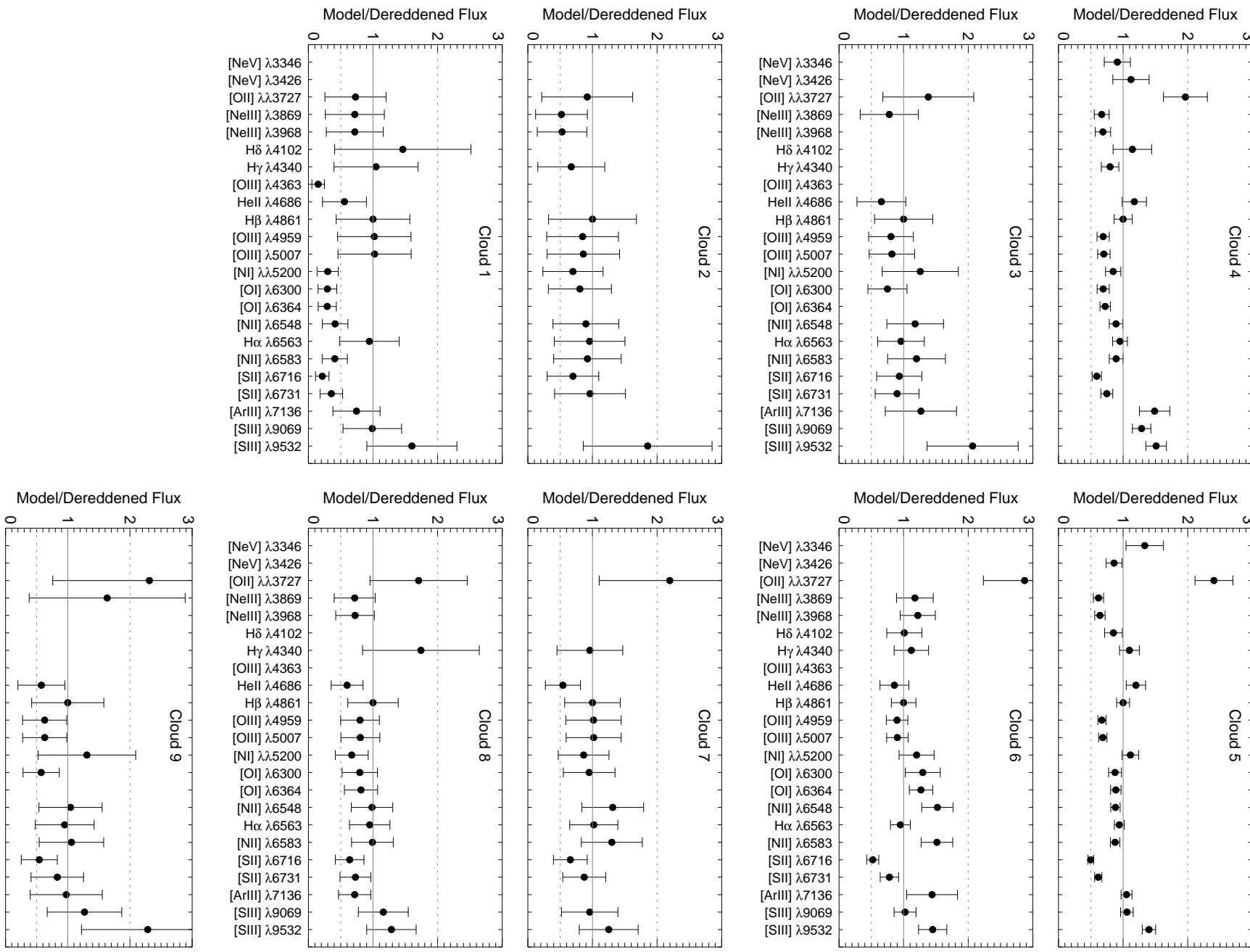
The photoionization models were generated using Cloudy's optimize command, where we allowed the ionization parameter,  $U$ , and total hydrogen density,  $n_H$ , to vary for each cloud. As previously discussed, our early photoionization model grids without optimization indicated that enhanced nitrogen abundances were required to fit the observed emission-line spectra. Therefore, the relative nitrogen abundance also was allowed to vary in the modelling procedure.

### 5.2. Model Results

The photoionization model results are presented in Figure 17, where we plot the ratio of the model predictions to the observed emission-line fluxes. With the exception of cloud 1, the vast majority of the emission lines are reproduced reasonably well (within a factor of two) by the models. Given the simplicity of the models and the limited number of input parameters, this agreement suggests that photoionization is the dominant ionization mechanism in most of the NLR clouds.

High-excitation  $[\text{Ne}\text{V}] \lambda 3346$  and  $[\text{Ne}\text{V}] \lambda 3426$  lines were detected in the spectra of the two NLR clouds closest to the nucleus (clouds 4 and 5). The highly-ionized  $[\text{Ne}\text{V}]$  emission lines have a large ionization potential (97.1 eV) and were not produced by our single-component, optically-thick (radiation bounded) photoionization models. The presence of these high-ionization emission lines indicates that an additional optically-thin (matter bounded) component is required in these clouds, similar to that found by studies of other Seyferts (Binette et al. 1996; Komossa & Schulz 1997; Kraemer et al. 2000). The two-component models were gen-

FIG. 17.— Ratios of the photoionization model predictions to the dereddened emission-line fluxes for each NLR cloud. The left-hand plots are for the NLR clouds south of nucleus, while those on the right are for the NLR clouds north of the nucleus. The radial distance from the nucleus increases as one moves from the top to bottom plots.



erated by assuming that all of the [Ne V] emission arises in the high-ionization matter-bounded component and that lower ionization lines (e.g. [O III], [O II], [N II], and [S II]) are produced in the radiation-bounded component. As before, these models were optimized in Cloudy by allowing the ionization parameter, total hydrogen density, and nitrogen abundance to vary. For the matter-bounded components, we also varied the total hydrogen column density, which controls the depth of the cloud. The resulting two-component models for clouds 4 and 5 are shown in Figure 17. Single-component, radiation-bounded models were used for all of the other NLR clouds. The model parameters used to generate the photoionization models for each cloud are presented in Table 6.

The model results show the presence of a gradient in both the ionization parameter and the nitrogen abundance. Excluding cloud 1, which is poorly fit by the photoionization models, the ionization parameter is larger for the clouds closest to the nucleus and decreases with increasing radial distance out to cloud 9 ( $\sim 2''$ , 80 pc). This result confirms the general trend observed earlier in the [O III]  $\lambda\lambda 5007$ /[O II]  $\lambda\lambda 3727$  and [O III]  $\lambda\lambda 5007$ /H $\beta$  emission-line ratios and is consistent with the radial dilution of a central ionizing radiation field in which the gas density decreases more slowly than  $r^{-2}$ . Interestingly, the photoionization model results also show a gradient in nitrogen abundance over the NLR region (Fig. 18). The nitrogen abundance appears to be larger closer to the nucleus ( $\sim 4.5$  N $_{\odot}$ ) and decreases with increasing radius, reaching  $\sim 3$  N $_{\odot}$  for the outer clouds.

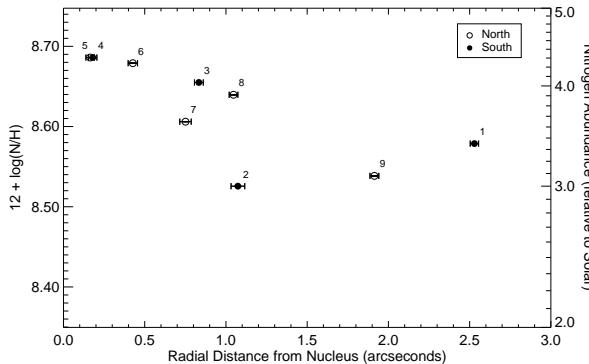


FIG. 18.— Nitrogen abundance (relative to solar) of the optimized Cloudy photoionization models for the NLR clouds.

Peimbert (1968) was the first to claim that solar abundances could not explain the observed emission-line ratios in the near-nuclear region of M51. His work suggested that nitrogen was overabundant in the nucleus of M51 ( $r \leq 3.5''$ ) by a factor of about five relative to solar. Later emission-line studies by Rose & Searle (1982) and Ford et al. (1985,  $\sim 19$  N $_{\odot}$  for the XNC) also inferred an enhancement of nitrogen in the circumnuclear region of M51. Our large [N II]  $\lambda\lambda 6548, 6583$ /H $\alpha$  ratios (2.8 – 6.2) confirm that nitrogen is enhanced in the NLR of M51.

Nitrogen overabundances on the scale inferred by us in M51 have also been claimed in studies of many Seyfert galaxies (Storchi-Bergmann & Pastoriza 1989, 1990; Dopita & Sutherland 1996; Storchi-Bergmann et al. 1998), LINERs (Binette 1985; Filippenko & Terlevich 1992), and starburst galaxies (Coziol et al. 1999). In particular, (Storchi-Bergmann & Pastoriza 1990) found that a range of nitrogen abundances, from 0.5 to 5 times solar, provided a

better fit to the the NLR emission-line ratios from a sample of 180 Seyfert 2s and LINERs. Of these galaxies, approximately one-third presented a nitrogen overabundance in the nucleus (Storchi-Bergmann 1991). These results suggest that nitrogen is overabundant in active nuclei whenever [N II]  $\lambda\lambda 6548, 6583$ /H $\alpha$   $> 1.5$ . The enrichment of nitrogen found in the nuclei of Seyferts may indicate that the N/O abundance gradient found in the disks of spiral galaxies (Searle 1971; Smith 1975; Vila Costas & Edmunds 1993) continues into the nuclear regions. Generally speaking, the selective enhancement of nitrogen may be caused by secondary CNO nucleosynthesis, in which nitrogen forms from preexisting carbon and oxygen (Thurston et al. 1996), and may be distributed by stellar winds from massive stars (Cid Fernandes et al. 1992).

### 5.3. Model Discrepancies

While the overall agreement of the simple photoionization model predictions and the observed optical spectrum generally is good, there are a few discrepancies. The poorest match occurs for the [O II]  $\lambda\lambda 3727$  emission line, which is generally overpredicted by the models. For three of the NLR clouds this discrepancy is within a factor of 2.5. The largest mismatch (a factor of  $\sim 3$ ) occurs for cloud 6. Although it is possible that our measured [O II] fluxes are low as a result of dereddening errors, additional dereddening would change the emission-line fluxes for the entire spectrum. In particular, the [Ne III]  $\lambda\lambda 3869, 3968$  lines, which are at a comparable wavelength to [O II]  $\lambda\lambda 3727$ , would also increase in strength counter to the model predictions. Given the generally good agreement of the models with the dereddened line fluxes, the discrepancy between the [O II]  $\lambda\lambda 3727$  model prediction and the dereddened [O II]  $\lambda\lambda 3727$  flux does not appear to be a result of dereddening errors.

One method to reduce the predicted [O II]  $\lambda\lambda 3727$  emission-line fluxes is to increase the total hydrogen density,  $n_H$ . [O II]  $\lambda\lambda 3727$  has a relatively low critical density of  $3.3 \times 10^3$  cm $^{-3}$ , above which the lines are collisionally suppressed. To examine this effect, we have generated photoionization models with increased total hydrogen density. While the [O II]  $\lambda\lambda 3727$  lines are indeed suppressed, the higher density models provide a poorer overall fit to the observed spectrum. In particular, [N I] and [S II] are suppressed and many lines, including [Ne III]  $\lambda 3869$ , [O III]  $\lambda 5007$ , [O I]  $\lambda 6300$ , and [S III]  $\lambda 9532$ , are overpredicted for these models. It is possible that our simple assumption of constant density clouds is invalid and that more complex models involving density stratification may provide a better fit for [O II]  $\lambda\lambda 3727$ . Or perhaps, the nitrogen overabundance described in § 5.2 is correlated with an oxygen underabundance.

We also find modest discrepancies for the [S III] and [S II] emission lines. [S III] is slightly overproduced (by a factor of  $\sim 1.4$ ) and [S II] is slightly underproduced (by a factor of  $\sim 1.4$ ) by the models. A general problem with photoionization models is that they overpredict the strength of the [S III]  $\lambda 9069$  and [S III]  $\lambda 9532$  lines (Ho et al. 1993; Kraemer et al. 2000). Osterbrock et al. (1992) suggested that this discrepancy may be improved with underabundances of sulfur, however, we note that the dielectronic recombination rates for sulfur are uncertain (Ali et al. 1991). While the [S III] lines are overpredicted, the [S II]  $\lambda 6716$  and [S II]  $\lambda 6731$  lines are a somewhat underpredicted. This in turn may suggest the presence of a overabundance of sulfur, which has been detected by Storchi-Bergmann & Pastoriza (1990) in a sample of 180

TABLE 6. PHOTOIONIZATION MODEL PARAMETERS

Cloud	$\log U$	Hydrogen Density ( $10^3 \text{ cm}^{-3}$ )	Column Density ( $10^{20} \text{ cm}^{-2}$ )	Nitrogen Abundance ( $N_{\odot}$ )	Note
1	-2.83	4.6	6.1	3.4	RB
2	-3.27	2.3	1.9	3.0	RB
3	-3.07	0.7	2.6	4.0	RB
4 <sup>a</sup>	-3.13	2.6	2.8	4.3	RB
	-1.52	1.0	0.8	4.3	MB
5 <sup>b</sup>	-2.90	1.8	4.6	4.3	RB
	-1.08	0.2	1.8	4.3	MB
6	-3.26	6.3	2.5	4.3	RB
7	-3.39	4.8	1.7	3.6	RB
8	-3.21	2.5	2.2	3.9	RB
9	-3.39	5.1	1.8	3.1	RB

NOTE. — RB: radiation bounded; MB: matter bounded.

<sup>a</sup>90% RB + 10% MB.

<sup>b</sup>80% RB + 20% MB.

Seyfert and LINER galaxies. Clearly, altering the sulfur abundances will not improve the fit for both [S III] and [S II]. However, the discrepancy in these lines is relatively modest.

As noted earlier, the photoionization models provide a poor match to the observed spectrum of cloud 1. This cloud also possesses the largest [O III]/H $\beta$  ratio, indicating the presence of high ionization. The proximity of this cloud to the entry point of the radio jet into the lobe suggests that shock excitation may be an important source of ionization. Previous studies (Ford et al. 1985; Cecil 1988; Terashima & Wilson 2001) have provided considerable evidence that shocks contribute to the ionization structure of the XNC in M51.

## 6. SHOCK IONIZATION MODELS

While it is widely held that the dominant source of energy input into the NLR gas is photoionization by a nonstellar nuclear continuum (Koski 1978; Osterbrock 1989), collisional shock wave heating may provide an additional source of ionization in the NLR (Morse et al. 1996; Bicknell et al. 1998; Wilson & Raymond 1999). Shock waves generated by supersonic radio ejecta would compress and heat the ambient gas and may contribute, at least locally, a significant fraction of the ionizing photons (Dopita & Sutherland 1995, 1996; Bicknell et al. 1998). These EUV photons are generated in the hot ( $T \sim 10^6 \text{ K}$ ) postshock cooling region and diffuse both upstream and downstream. The photons diffusing downstream influence the ionization of the shock recombination region, while those diffusing upstream ionize the preshock medium.

Dopita & Sutherland (1995, 1996) have created a low-density grid of fast radiative shock models using the code MAPPINGS II. The models assume a steady-state one-dimensional radiative flow with roughly solar abundances. Dopita & Sutherland (1995, 1996) emphasized the importance of the EUV photons that diffuse upstream into the preshock gas and produce a high ionization precursor region. We refer to the MAPPINGS II shock models that include the postshock cooling and photoionized gas as “shock-only” models, while those that include contributions from both the shocked gas and the ionized precursor region as “shock + precursor” models. Current, publicly available, shock models are limited because they represent a one-dimensional model of a more complex three-dimensional shock structure (Dopita & Sutherland 1996).

The two most important parameters in controlling the emergent

shock spectrum are the shock velocity,  $v_s$ , and the magnetic parameter,  $B/n^{1/2}$ . The shock velocity controls the shape of the ionizing continuum, and the magnetic parameter controls the effective ionization parameter of the postshock recombination zone (Dopita & Sutherland 1995, 1996). The MAPPINGS II model grids are computed for shock velocities in the range of  $v_s = 150 - 500 \text{ km s}^{-1}$  and magnetic parameters  $B/n^{1/2} = 0 - 4 \mu\text{G cm}^{3/2}$ . Magnetic parameters  $B/n^{1/2} \sim 2 - 4 \mu\text{G cm}^{3/2}$  correspond to the equipartition of the magnetic and thermal pressures in the preshock medium (Dopita & Sutherland 1996).

We have compared our observed NLR line ratios with the MAPPINGS II shock models to determine if shocks play a significant role in the excitation of the NLR gas. As demonstrated earlier with the Cloudy photoionization models, there appears to be an overabundance of nitrogen in the near-nuclear region of M51. Similarly, we find that the solar abundance MAPPINGS II model grids cannot reproduce the large observed [N II]/H $\alpha$  ratios of the NLR clouds in M51. For a sample of active galaxies, Dopita & Sutherland (1996) observed [N II]/H $\alpha$  ratios that were  $\sim 0.4$  dex larger than the solar abundance MAPPINGS II shock model grids. These authors likewise suggested that this discrepancy was due to an enhancement of the nitrogen abundance and generated new shock models with a N/O abundance of two times solar. They found a nearly one-to-one increase in the strength of the [N II] lines with the scaled abundance. Thus to approximate the effect of nitrogen enhancement in M51, we scaled the MAPPINGS II nitrogen emission-line fluxes ([N I] and [N II]) by the relative nitrogen overabundance.

The MAPPINGS II shock-only models are ruled out for all of our NLR clouds because they fail to predict the observed [O II] $\lambda\lambda 3727/\text{[O II]} \lambda 5007$  and [O III] $\lambda 5007/\text{H}\beta$  line ratios. The M51 [O II] $\lambda\lambda 3727/\text{[O III]} \lambda 5007$  line ratios lie in the range 0.1–1.1, while the shock-only models predict [O II] $\lambda\lambda 3727/\text{[O III]} \lambda 5007 > 3$ . This is not a surprising result as the shock-only models generally lie in the region occupied by LINER galaxies (Dopita & Sutherland 1995; Dopita et al. 1997).

However, the MAPPINGS II shock+precursor models can reproduce the observed [O II] $\lambda\lambda 3727/\text{[O III]} \lambda 5007$  and [O III] $\lambda 5007/\text{H}\beta$  line ratios for shock velocities in the range  $300 - 500 \text{ km s}^{-1}$  ( $T_X \approx 1.3 - 3.5 \times 10^6 \text{ K}$ ), consistent with results for several

other Seyfert galaxies (Dopita & Sutherland 1995; Allen et al. 1999; Ferruit et al. 1999b; Evans et al. 1999). Unfortunately, for shock velocities in this range there is considerable overlap of the shock+precursor and photoionization model grids for most of the optical emission lines. As such, optical emission lines generally are unable to provide conclusive discrimination between shock and photoionization models (e.g., Dopita & Sutherland 1995; Allen et al. 1999; Evans et al. 1999). However, shocks provide a rich, collisionally-excited UV spectrum, many of whose lines are predicted to be much stronger than that found by photoionization models (Dopita & Sutherland 1996; Allen et al. 1998). Because of this, Allen et al. (1998) emphasized the importance of ultraviolet emission lines, such as  $\text{N}\text{II}\lambda 991$ ,  $\text{C}\text{IV}\lambda\lambda 1549$ ,  $\text{He}\text{II}\lambda 1640$ ,  $\text{C}\text{III}\lambda 1909$ , and  $\text{C}\text{II}\lambda 2326$ , in distinguishing between shock and photoionization models. Unfortunately, the ultraviolet emission in M51 is very weak, and a sensitive UV spectrum of the near-nuclear region of M51 does not exist. Furthermore, the available *IUE* UV spectrum only shows a blended  $\text{Si}\text{III}\lambda 1892$  and  $\text{C}\text{III}\lambda 1909$  emission line, which has been attributed to  $\text{H}\text{II}$  regions located within the large  $10'' \times 20''$  aperture (Ellis et al. 1982).

Without UV emission lines, the best diagnostic we have available to differentiate between the shock+precursor and photoionization models is  $[\text{O}\text{III}]\lambda 5007/\text{H}\beta$  vs.  $[\text{O}\text{I}]\lambda 6300/\text{H}\alpha$  (Fig. 19). As shown in Fig. 19, shock+precursor models with shock velocities  $v_s \gtrsim 300 \text{ km s}^{-1}$  predict a stronger  $[\text{O}\text{I}]\lambda 6300/\text{H}\alpha$  ratio than our photoionization models. Overall, our observed  $[\text{O}\text{I}]\lambda 6300/\text{H}\alpha$  line ratios appear to be more consistent with the photoionization model grids. Excluding clouds 1, 9, and 7, the shock+precursor models overpredict the strength of the  $[\text{O}\text{I}]\lambda 6300/\text{H}\alpha$  ratio by factors of 2–6, effectively ruling out the shock+precursor models for these clouds.

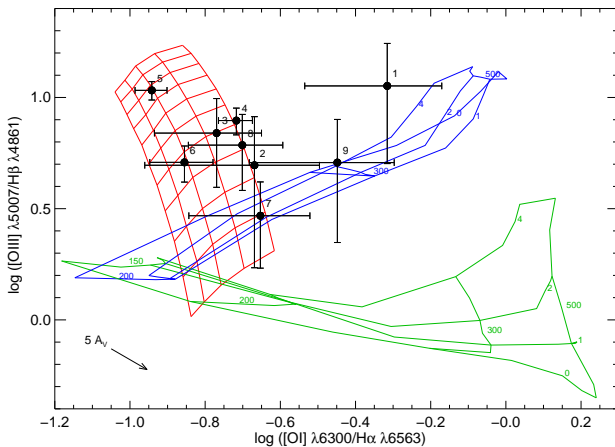


FIG. 19.— $[\text{O}\text{III}]\lambda 5007/\text{H}\beta$  vs.  $[\text{O}\text{I}]\lambda 6300/\text{H}\alpha$  for the NLR clouds overplotted with the MAPPINGS II shock-only (green), shock+precursor (blue) and Cloudy model grids with  $4\times$  solar nitrogen (red). The MAPPINGS II model grids are labeled with shock velocity in units of  $\text{km s}^{-1}$  (shock-only: 150–500  $\text{km s}^{-1}$ , shock+precursor: 200–500  $\text{km s}^{-1}$ ) and magnetic parameter  $B/n^{1/2}$  (0–4) in units of  $\mu\text{G cm}^{3/2}$ . The Cloudy photoionization model grid spans  $\log U$  in the range  $-3.5$  to  $-2.5$  (bottom to top) and  $\log n_H$  from  $2$  to  $4 \text{ cm}^{-3}$  (left to right).

While the shock+precursor models are able to predict the strength of the  $[\text{O}\text{I}]\lambda 6300/\text{H}\alpha$  ratio in clouds 7 and 9, they fail to provide a good fit for all of the observed emission lines. For cloud 7, the best overall fit shock+precursor

model is for  $v_s = 250 \text{ km s}^{-1}$  and  $B/n^{1/2} = 1 \mu\text{G cm}^{3/2}$ . However, in this model the strength of the high ionization  $\text{He}\text{II}\lambda 4686/\text{H}\beta$  ratio is underpredicted by a factor of five. The  $\text{He}\text{II}\lambda 4686/\text{H}\beta$  prediction is improved by increasing the shock velocity to  $350 \text{ km s}^{-1}$ , but the  $[\text{O}\text{I}]\lambda 6300/\text{H}\beta$  and  $[\text{N}\text{I}]\lambda\lambda 5200/\text{H}\beta$  ratios are overproduced by a factor of  $\sim 3$  and the  $[\text{O}\text{III}]\lambda 5007/\text{H}\beta$  and  $[\text{O}\text{II}]\lambda\lambda 3727/\text{H}\beta$  ratios are overproduced by factors  $\gtrsim 2$ . Turning to cloud 9, the best overall shock+precursor model fit is also for  $v_s = 250 \text{ km s}^{-1}$  and  $B/n^{1/2} = 1 \mu\text{G cm}^{3/2}$ . While this model provides the lowest  $\chi^2$ , many of the emission lines, including  $[\text{Ne}\text{III}]\lambda 3869$ ,  $[\text{O}\text{III}]\lambda 5007$ , and  $[\text{N}\text{II}]\lambda 6583$  (even with  $3.1 N_{\odot}$ ), are underproduced by factors of  $\sim 2$ , and  $\text{He}\text{II}\lambda 4686$  is underproduced by a factor of four. The fit appears to be influenced by the relatively strong observed  $[\text{O}\text{II}]\lambda\lambda 3727$ ,  $[\text{Ne}\text{III}]\lambda 3869$ ,  $[\text{N}\text{I}]\lambda\lambda 5200$ , and  $[\text{O}\text{I}]\lambda 6300$  emission lines. Excluding these lines from the  $\chi^2$  calculation, we find the best shock+precursor model parameters are  $v_s = 350 \text{ km s}^{-1}$  and  $B/n^{1/2} = 1 \mu\text{G cm}^{3/2}$ . While this model provides an improved fit for most of the emission lines,  $[\text{N}\text{I}]\lambda\lambda 5200$  is overproduced by a factor of four and  $[\text{O}\text{II}]\lambda\lambda 3727$ ,  $[\text{O}\text{I}]\lambda 6300$ , and  $[\text{Ne}\text{III}]\lambda 3869$  are overproduced by  $\sim 2$ . There does not appear to be a particular combination of  $v_s$  and  $B/n^{1/2}$  that provides a good fit to all of the emission lines in cloud 9. While shocks cannot necessarily be ruled out in clouds 7 and 9 based on our optical emission-line data, we find that our photoionization models provide a better overall fit to these NLR clouds than the shock+precursor models.

### 6.1. Cloud 1

In contrast, we find that shocks are important for cloud 1. As discussed in § 5.3, photoionization models do not provide a good fit to observed optical spectrum of cloud 1 (see Fig 17). However, the MAPPINGS II shock+precursor models provide a reasonable fit to the observed emission lines in this cloud. The best fit shock+precursor models have parameters in the range  $v_s = 400$ – $450 \text{ km s}^{-1}$  and  $B/n^{1/2} = 2$ – $4 \mu\text{G cm}^{3/2}$  with scaled nitrogen abundances of  $\sim 3.5$ . In Fig. 20 we plot the ratio of the  $v_s = 450 \text{ km s}^{-1}$  and  $B/n^{1/2} = 4 \mu\text{G cm}^{3/2}$  shock+precursor model predictions to the observed emission-line fluxes in cloud 1. For comparison, we have also overplotted the optimized Cloudy photoionization model results for this cloud. In particular, the shock+precursor models produce a better match to the  $[\text{N}\text{I}]\lambda\lambda 5200$ ,  $[\text{O}\text{I}]\lambda 6300$ , and  $[\text{O}\text{I}]\lambda 6364$  lines than the photoionization models, which underproduce these emission lines by factors of  $\sim 3$ . In Table 7, we compare the optical spectrum of cloud 1 with the shock+precursor model predictions for the full range of shock velocities and magnetic parameters.

For a fully ionized gas with solar helium abundances, the predicted postshock temperature can be estimated as  $T_s = 1.4 \times 10^5 v_{s100}^2 \text{ K}$ , where  $v_{s100}$  is the shock velocity in units of  $100 \text{ km s}^{-1}$  (Hollenbach & McKee 1979). For shock velocities in the range  $v_s = 400$ – $450 \text{ km s}^{-1}$ , we derive postshock temperatures in the range from  $2.2$ – $2.8 \times 10^6 \text{ K}$ . These values are roughly consistent with the X-ray temperature of  $T_X = 6.7 \times 10^6 \text{ K}$  obtained from *Chandra* observations of the XNC (Terashima & Wilson 2001), providing further evidence that shocks are important for the excitation of cloud 1, which lies near the northern edge of the XNC.

We do not find evidence of a broad  $[\text{O}\text{III}]\lambda 5007$  velocity dispersion for cloud 1. However, because this line is produced primarily in the shock precursor region, this may be expected.

TABLE 7. LINE RATIOS FOR CLOUD 1 AND MAPPINGS II SHOCK+PRECURSOR MODELS

Line <sup>a</sup>	Cloud 1 <sup>b</sup>	Shock+Precursor Models				
		200 km s <sup>-1</sup>	300 km s <sup>-1</sup>	400 km s <sup>-1</sup>	450 km s <sup>-1</sup>	500 km s <sup>-1</sup>
[O II] $\lambda\lambda 3727$	4.39 (2.85)	2.29–3.64	1.69–5.19	1.73–6.97	1.70–7.14	1.70–7.19
[Ne III] $\lambda 3869$	1.46 (0.93)	0.18–0.21	0.37–0.58	0.71–1.13	0.93–1.36	1.16–1.59
[Ne III] $\lambda 3968$	0.44 (0.27)	~0.06	0.11–0.18	0.22–0.35	0.29–0.42	0.36–0.49
H $\delta$ $\lambda 4102$	0.18 (0.13)	~0.25	0.25–0.26	~0.26	~0.26	~0.26
H $\gamma$ $\lambda 4340$	0.45 (0.28)	~0.46	~0.46	0.46–0.47	~0.47	0.46–0.47
[O III] $\lambda 4363^c$	0.04 (0.03)	0.03–0.04	~0.01	~0.01	~0.01	~0.01
He II $\lambda 4686$	0.41 (0.25)	~0.05	0.15–0.20	0.27–0.36	0.25–0.33	0.23–0.31
H $\beta$ $\lambda 4861$	1.00 (0.57)	1.00	1.00	1.00	1.00	1.00
[O III] $\lambda 4959$	3.92 (2.18)	0.53–0.55	1.54–1.70	2.78–3.15	3.59–4.03	4.19–4.78
[O III] $\lambda 5007$	11.27 (6.23)	1.53–1.58	4.44–4.90	8.01–9.09	10.33–11.59	12.08–13.76
[N I] $\lambda\lambda 5200$	0.80 (0.44)	0.17–0.27	0.56–0.80	0.87–1.33	1.07–1.50	1.39–1.64
[O I] $\lambda 6300$	1.49 (0.73)	0.22–0.40	0.89–1.31	1.68–2.38	1.87–2.53	2.37–2.76
[O I] $\lambda 6364$	0.48 (0.23)	0.07–0.13	0.29–0.42	0.54–0.77	0.60–0.82	0.76–0.89
[N II] $\lambda 6548$	4.79 (2.29)	0.68–1.46	0.82–2.26	1.17–2.86	1.28–2.95	1.34–2.94
H $\alpha$ $\lambda 6563$	3.09 (1.51)	2.99–3.02	2.92–2.95	2.90–2.91	2.90–2.91	2.89–2.92
[N II] $\lambda 6583$	14.33 (6.85)	2.01–4.31	2.40–6.66	3.44–8.41	3.77–8.69	3.93–8.66
[S II] $\lambda 6716$	1.90 (0.92)	0.29–0.56	0.58–0.91	0.81–1.21	0.78–1.16	0.82–1.11
[S II] $\lambda 6731$	1.71 (0.84)	0.25–0.41	0.49–0.70	0.58–1.14	0.57–1.23	0.59–1.27
[Ar III] $\lambda 7136$	0.49 (0.24)	0.08–0.11	0.11–0.20	0.10–0.23	0.09–0.23	0.09–0.22
[S III] $\lambda 9069$	0.96 (0.44)	0.24–0.33	0.25–0.49	0.24–0.56	0.24–0.60	0.25–0.65
[S III] $\lambda 9532$	1.47 (0.64)	0.59–0.80	0.60–1.18	0.59–1.37	0.59–1.45	0.60–1.58

NOTE. — The range of values in columns 3–7 correspond to the range of magnetic parameters  $B/n^{1/2} = 0–4 \mu\text{G cm}^{3/2}$ . The nitrogen lines have been scaled by 3.5 to approximate the effect of an overabundance of nitrogen.

<sup>a</sup>Normalized to H $\beta$  unless otherwise indicated.

<sup>b</sup>Dereddened fluxes with errors shown in parenthesis.

<sup>c</sup>[O III]  $\lambda 4363$ /[O III]  $\lambda 5007$  electron temperature ratio.

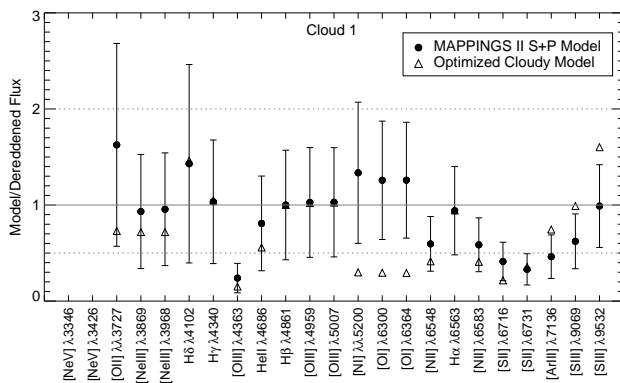


FIG. 20.—Ratios of the MAPPINGS II shock+precursor model predictions and the optimized Cloudy photoionization model predictions to the dereddened emission-line fluxes of cloud 1. The MAPPINGS II shock+precursor model is for  $v_s = 450 \text{ km s}^{-1}$  and  $B/n^{1/2} = 4 \mu\text{G cm}^{3/2}$  with the nitrogen lines scaled by 3.5 to approximate the effect of nitrogen overabundance.

For lines which are produced in the postshock region, such as [O II]  $\lambda\lambda 3727$ , [O III]  $\lambda 4363$ , and [Ne V]  $\lambda 3426$ , we only have lower spectral resolution data and are therefore unable to determine if the velocity widths are broader for these lines.

The largest discrepancies between the MAPPINGS II shock+precursor model and the observed spectrum of cloud 1 are the underprediction of the [S II] and [O III]  $\lambda 4363$  emission lines. As the [S III]  $\lambda 9069$  emission line also is slightly underpredicted, it appears the model fit could be improved with a modest overabundance ( $\sim 2 \times$  solar) of sulfur. An overabundance of sulfur previously has been found in a sample of Seyferts and LINERs and may be correlated with the nitrogen enhancement (Storchi-Bergmann & Pastoriza 1989,

1990; Schmitt et al. 1994). However, the discrepancy with the [S II] lines may be a result of the incomplete dielectronic recombination rates for sulfur (Ali et al. 1991).

While the [O III]  $\lambda 4363$ /[O III]  $\lambda 5007$  ratio is underpredicted in cloud 1, this appears to be a general feature of the MAPPINGS II shock+precursor models (Dopita & Sutherland 1995). This is especially true for shock velocities  $v_s \gtrsim 300 \text{ km s}^{-1}$ , in which the majority of the [O III] emission is produced in the lower-temperature photoionized precursor rather than the hot postshock region (Sutherland et al. 1993; Dopita & Sutherland 1995, 1996). The [O III]  $\lambda 4363$ /[O III]  $\lambda 5007$  prediction is improved with shock-only or low-velocity shock+precursor models, however, these models provide a much worse overall fit to the ensemble of emission lines (see Table 7). In any case, the MAPPINGS II shock+precursor models match the observed optical spectrum of cloud 1 better than the photoionization models (see Fig. 20).

## 6.2. H $\beta$ Luminosity

Correcting for the distance to M51 (8.4 Mpc), the observed cloud 1 H $\beta$  luminosity is  $2.7 \times 10^{36} \text{ erg s}^{-1}$ . The H $\beta$  luminosity predicted from the shock+precursor models is given by Dopita & Sutherland (1995) as

$$L(\text{H}\beta) = A n_0 \left[ 7.44 \times 10^{-6} \left( \frac{v_s}{100 \text{ km s}^{-1}} \right)^{2.41} + 9.85 \times 10^{-6} \left( \frac{v_s}{100 \text{ km s}^{-1}} \right)^{2.28} \right], \quad (4)$$

where  $A$  is the shock area ( $\text{cm}^{-2}$ ) and  $n_0$  ( $\text{cm}^{-3}$ ) is the preshock density. Because the cloud 1 shock is viewed nearly edge on (see § 3.1), we follow the examples of Ferruit et al. (1999a) and Schmitt et al. (2002) and estimate the shock area by assuming a line-of-sight depth equal to the slit width (0.19,

8 pc). For this cylindrical symmetry we derive a shock area of  $4.5 \times 10^{38} \text{ cm}^{-2}$  (47 pc $^2$ ). We estimate the preshock density using the shock compression factors for the [S II] zone computed by Ferruit et al. (1999a). For the best-fitting shock velocities in the range from 400–450 km s $^{-1}$  these compression factors are 46.4–50. Given the calculated [S II] electron density of 490 cm $^{-3}$  for cloud 1, the resulting preshock densities are in the range from 9.8–10.6 cm $^{-3}$ . For shock velocities  $v_s = 400–450 \text{ km s}^{-1}$ , the shock+precursor model predicts H $\beta$  luminosities in the range  $L(\text{H}\beta) = 2.1–2.6 \times 10^{36} \text{ erg s}^{-1}$ , which is approximately 78–96% of the observed H $\beta$  luminosity of cloud 1. This suggests that, within the uncertainties in the preshock density and the estimated shock velocity, shocks are the dominant excitation mechanism in cloud 1.

## 7. SUMMARY

We have examined the physical conditions in the NLR of M51 using archival *HST*/WFPC2 narrowband images, high spatial resolution, long-slit *HST*/STIS spectra, and VLA 8.4 GHz radio continuum maps. Our velocity measurements of the NLR clouds show that the radial velocity distribution is inconsistent with gravitational rotation in a circumnuclear disk. The kinematics are consistent with radial outflows from the nucleus that lie nearly in the plane of the sky. On the southern side of the nucleus, the radial velocities of the NLR clouds appear to be influenced by the presence of the southern radio jet.

Through the use of standard line-ratio diagnostics, we have shown that the emission-line ratios in the NLR clouds are in agreement with those typically found in Seyfert galaxies. The ionization state of the gas, as probed by the [O III]/H $\beta$  and [O III]/[O II] line ratios, decreases radially from the nucleus out to  $r \sim 2''$ . This is consistent with photoionization from a nonstellar nuclear continuum source in which the density falls off more gradually than  $r^{-2}$ . The ionization is larger for cloud 1 ( $r = 2.5''$ ) and appears to be caused by the presence of shocks.

The [S II]  $\lambda 6716/\lambda 6731$  flux ratios indicate that the average electron density within the NLR gas is  $\sim 770 \text{ cm}^{-3}$ . Given the large error bars for the [S II] fluxes, no radial trend can be inferred for the electron density. Cloud 1 is the only cloud in which we detected [O III]  $\lambda 4363$ . The derived [O III] electron temperature is 24,000 K. This, coupled with our radio observations, suggests that shocks are an important heating mechanism for this cloud. Upper limits to the [O III] electron temperature for clouds 4, 5, 6, and 8 ( $T_e \lesssim 11,000 \text{ K}$ ) indicate that collisional heating is less important for these clouds. These electron temperatures are consistent with photoionization.

The optical and 3.6 cm radio emission both exhibit an extended, knotty emission structure along a position angle of 170°. Our 3.6 cm data are in agreement with the earlier 6 cm observations of Crane & van der Hulst (1992). Both observations exhibit a weak southern jet,  $\sim 2.5''$  in extent, that connects with a diffuse lobe structure south of the nucleus. The well-known XNC optical structure south of the nucleus appears to be coincident with the southern radio lobe. The higher spatial resolution 3.6 cm data exhibit several knots of emission, indicating that there is structure in the jet. In general, these radio knots lie adjacent to the observed optical clouds, suggesting that the radio jet may contribute to the kinematics or ionization structure of the optical emission. Cloud 1, at the northern edge of the XNC, appears to lie near, but west of, the entry point of the jet into the southern ra-

dio lobe. Recent *Chandra* observations (Terashima & Wilson 2001) also detect X-ray emission coincident with the XNC.

At the assumed entry point of the radio jet into the diffuse lobe structure, we find both radio and optical emission. The optical emission, cloud 1, is straddled by two radio knots, R0 and R1. The proximity of cloud 1 with the jet-lobe entry point and radio knots R0 and R1 suggests that collisional excitation may be important for this cloud.

Cloud-by-cloud photoionization models were generated to determine the relative importance of photoionization for each cloud. With the exception of cloud 1, the photoionization models provide good fits to the NLR emission-line clouds. However, our models require supersolar nitrogen abundances to match the dereddened [N I]  $\lambda\lambda 5200$ , [N II]  $\lambda 6548$ , and [N II]  $\lambda 6583$  line ratios. This result is supported by other studies of Seyfert galaxies that also required selective enhancement of nitrogen by factors up to five times solar to fit the observed nitrogen emission. In addition, we find a strong gradient in the nitrogen abundance in the near-nuclear region. The nitrogen abundance is  $\sim 4.5 \text{ N}_\odot$  for the near-nuclear clouds ( $r \sim 0.2''$ ) and decreases for increasing radial distance to  $\sim 3 \text{ N}_\odot$  for the outer clouds ( $r \sim 2''$ ).

We also find a gradient in ionization parameter, which agrees with the result inferred from the observed emission-line ratios. We detect the highly-ionized [Ne V]  $\lambda 3346$  and [Ne V]  $\lambda 3426$  emission lines in clouds 4 and 5 ( $r \sim 0.2''$ ), which indicates the presence of a high-ionization matter-bounded component. We successfully modelled these clouds with two-component models, which included contributions from both matter-bounded and radiation-bounded components.

The photoionization models do not provide a good fit to the observed optical spectrum of cloud 1. Given the prior evidence that shocks contribute to the ionization structure of the XNC (Ford et al. 1985; Cecil 1988), we compared the emission-line fluxes of cloud 1 with MAPPINGS II shock model grids (Dopita & Sutherland 1995, 1996). The MAPPINGS II shock+precursor models with velocities in the range  $v_s = 400–450 \text{ km s}^{-1}$ , magnetic parameters  $B/n^{1/2} = 2–4 \mu\text{G cm}^{3/2}$ , and scaled nitrogen abundances of  $\sim 3.5$  provide a reasonable fit to the observed emission lines in this cloud. Later *Chandra* X-ray observations by Terashima & Wilson (2001) further support the conclusion that shocks are the dominant source of ionization at the location of cloud 1.

## 8. CONCLUSIONS

The optical and radio morphologies in the NLR of M51 exhibit a striking correspondence. The conical, limb-brightened optical morphology south of the nucleus is suggestive of evacuation by the weak southern radio jet. The near coincidence of the bright optical emission clouds with the position angle of the radio jet and the proximity of the optical and radio knots also suggest that the radio jet may influence the kinematic and ionization structure of the optical emission.

We find that, in general, photoionization is the dominant excitation mechanism for the brightest optical emission-line clouds. However, shock+precursor models provide the best fit to the optical emission-line cloud that lies near, but west of, the entry point of the jet into the diffuse radio lobe. Thus, shocks are an important excitation mechanism for at least some regions in the NLR of M51. Furthermore, we find some evidence for the presence of weak, higher velocity dispersion clouds. Several [O III] clouds were not well fit by a single Gaussian and required a second, broader Gaussian

emission component to obtain a good fit. The signal-to-noise and general spectral resolution of our data were insufficient to permit a more detailed analysis of this diffuse emission. Higher signal-to-noise, higher spectral resolution STIS data (Ferruit et al., in preparation) that map the optical emission with four slit positions will help determine if shocks play a more pervasive role in the NLR of this Seyfert galaxy. Additionally, higher signal-to-noise and higher spatial resolution radio maps would be beneficial in determining the importance of weak radio jet structures, observed in several Seyfert galaxies, to the general AGN paradigm.

Support for these observations was provided by NASA

contract NAS5-30403 to LDB and MEK. Support for WAB was provided by Westerbork Observatory, which is operated by ASTRON (Netherlands Foundation for Research in Astronomy) with support from the Netherlands Foundation for Scientific Research (NWO). This research has made use of NASA's Astrophysics Data System Bibliographic Services. This research has also made use of the NASA/IPAC Extragalactic Database (NED), which is operated by the Jet Propulsion Laboratory, California Institute of Technology, under contract with the National Aeronautics and Space Administration.

## REFERENCES

Ali, B., Blum, R. D., Bumgardner, T. E., Cranmer, S. R., Ferland, G. J., Haefner, R. I., & Tiede, G. P. 1991, PASP, 103, 1182

Allen, M. G., Dopita, M. A., & Tsvetanov, Z. I. 1998, ApJ, 493, 571

Allen, M. G., Dopita, M. A., Tsvetanov, Z. I., & Sutherland, R. S. 1999, ApJ, 511, 686

Baldwin, J. A., Phillips, M. M., & Terlevich, R. 1981, PASP, 93, 5

Bica, E., & Alloin, D. 1986, A&A, 162, 21

Bicknell, G. V., Dopita, M. A., Tsvetanov, Z. I., & Sutherland, R. S. 1998, ApJ, 495, 680

Binette, L. 1985, A&A, 143, 334

Binette, L., Wilson, A. S., & Storchi-Bergmann, T. 1996, A&A, 312, 365

Brocklehurst, M. 1971, MNRAS, 153, 471

Capetti, A., Axon, D. J., Macchetto, F., Sparks, W. B., & Boksenberg, A. 1996, ApJ, 469, 554

Carrillo, R., Masegosa, J., Dultzin-Hacyan, D., & Ordoñez, R. 1999, Revista Mexicana de Astronomía y Astrofísica, 35, 187

Cecil, G. 1988, ApJ, 329, 38

Cid Fernandes, R., Dottori, H. A., Gruenwald, R. B., & Viegas, S. M. 1992, MNRAS, 255, 165

Condon, J. J. 1992, ARA&A, 30, 575

Coziol, R., Reyes, R. E. C., Considère, S., Davoust, E., & Contini, T. 1999, A&A, 345, 733

Crane, P. C., & van der Hulst, J. M. 1992, AJ, 103, 1146

Crenshaw, D. M., & Kraemer, S. B. 2000, ApJ, 532, L101

de Bruyn, A. G., & Wilson, A. S. 1978, A&A, 64, 433

de Vaucouleurs, G., de Vaucouleurs, A., Corwin, J. R., Buta, R. J., Paturel, G., & Fouque, P. 1991, Third Reference Catalogue of Bright Galaxies (New York: Springer-Verlag)

Delisle, S., & Hardy, E. 1992, AJ, 103, 711

Dopita, M. A., Koratkar, A. P., Allen, M. G., Tsvetanov, Z. I., Ford, H. C., Bicknell, G. V., & Sutherland, R. S. 1997, ApJ, 490, 202

Dopita, M. A., & Sutherland, R. S. 1995, ApJ, 455, 468

—. 1996, ApJS, 102, 161

Ellis, R. S., Gondhalekar, P. M., & Efstathiou, G. 1982, MNRAS, 201, 223

Evans, I., Koratkar, A., Allen, M., Dopita, M., & Tsvetanov, Z. 1999, ApJ, 521, 531

Evans, I. N., Tsvetanov, Z., Kriss, G. A., Ford, H. C., Caganoff, S., & Koratkar, A. P. 1993, ApJ, 417, 82

Falcke, H., Wilson, A. S., & Simpson, C. 1998, ApJ, 502, 199

Feldmeier, J. J., Ciardullo, R., & Jacoby, G. H. 1997, ApJ, 479, 231

Ferland, G. J., Korista, K. T., Verner, D. A., Ferguson, J. W., Kingdon, J. B., & Verner, E. M. 1998, PASP, 110, 761

Ferland, G. J., & Osterbrock, D. E. 1986, ApJ, 300, 658

Ferruit, P., Wilson, A. S., Falcke, H., Simpson, C., Pécontal, E., & Durret, F. 1999a, MNRAS, 309, 1

Ferruit, P., Wilson, A. S., Whittle, M., Simpson, C., Mulchaey, J. S., & Ferland, G. J. 1999b, ApJ, 523, 147

Filippenko, A. V., & Sargent, W. L. W. 1985, ApJS, 57, 503

Filippenko, A. V., & Terlevich, R. 1992, ApJ, 397, L79

Fitzpatrick, E. L. 1999, PASP, 111, 63

Ford, H., Tsvetanov, Z., & Kriss, G. 1996, BAAS, 188, No. 16.02

Ford, H. C., Crane, P. C., Jacoby, G. H., Lawrie, D. G., & van der Hulst, J. M. 1985, ApJ, 293, 132

Grevesse, N., & Anders, E. 1989, in AIP Conf. Proc. 183: Cosmic Abundances of Matter, ed. C. J. Waddington (New York: AIP), 1

Grillmair, C. J., Faber, S. M., Lauer, T. R., Hester, J. J., Lynds, C. R., & O'Neil, E. J. 1997, AJ, 113, 225

Heckman, T. M. 1980, A&A, 87, 152

Heckman, T. M., Miley, G. K., van Breugel, W. J. M., & Butcher, H. R. 1981, ApJ, 247, 403

Ho, L. C., Filippenko, A. V., & Sargent, W. L. W. 1993, ApJ, 417, 63

—. 1997, ApJS, 112, 315

Hollenbach, D., & McKee, C. F. 1979, ApJS, 41, 555

Hutchings, J. B., Crenshaw, D. M., Kaiser, M. E., Kraemer, S. B., Weistrop, D., Baum, S., Bowers, C. W., Feinberg, L. D., Green, R. F., Gull, T. R., Hartig, G. F., Hill, G., & Lindler, D. J. 1998, ApJ, 492, L115

Kaiser, M. E., Bradley, L. D., Hutchings, J. B., Crenshaw, D. M., Gull, T. R., Kraemer, S. B., Nelson, C. H., Ruiz, J., & Weistrop, D. 2000, ApJ, 528, 260

Komossa, S., & Schulz, H. 1997, A&A, 323, 31

Kormendy, J., Bender, R., Ajhar, E. A., Dressler, A., Faber, S. M., Gebhardt, K., Grillmair, C., Lauer, T. R., Richstone, D., & Tremaine, S. 1996, ApJ, 473, L91

Koski, A. T. 1978, ApJ, 223, 56

Kraemer, S. B., Crenshaw, D. M., Hutchings, J. B., Gull, T. R., Kaiser, M. E., Nelson, C. H., & Weistrop, D. 2000, ApJ, 531, 278

Kraemer, S. B., Ruiz, J., & Crenshaw, D. M. 1998, ApJ, 508, 232

Kurucz, R. 1993, ATLAS9 Stellar Atmosphere Programs and 2 km/s Grid. Kurucz CD-ROM No. 13 (Cambridge, MA: Smithsonian Astrophysical Observatory)

McCall, M. L., Rybski, P. M., & Shields, G. A. 1985, ApJS, 57, 1

Morse, J. A., Raymond, J. C., & Wilson, A. S. 1996, PASP, 108, 426

Osterbrock, D. E. 1989, Astrophysics of Gaseous Nebulae and Active Galactic Nuclei (Mill Valley, CA: University Science Books)

Osterbrock, D. E., Tran, H. D., & Veilleux, S. 1992, ApJ, 389, 196

Panagia, N., Capetti, A., Scuderi, S., Lamers, H., & Kirshner, R. P. 1996, in ASSL Vol. 209: New Extragalactic Perspectives in the New South Africa, ed. D. L. Block & J. M. Greenberg (Dordrecht: Kluwer Academic Publishers), 552

Peimbert, M. 1968, ApJ, 154, 33

Penston, M. V., et al. 1990, A&A, 236, 53

Peterson, B. M. 1997, An Introduction to Active Galactic Nuclei (Cambridge: Cambridge Univ. Press)

Pickles, A. J. 1998, PASP, 110, 863

Pogge, R. W. 1988, ApJ, 328, 519

Pogge, R. W., & de Robertis, M. M. 1995, ApJ, 451, 585

Rose, J. A., & Cecil, G. 1983, ApJ, 266, 531

Rose, J. A., & Searle, L. 1982, ApJ, 253, 556

Ruiz, J., Crenshaw, D. M., Kraemer, S. B., Bower, G. A., Gull, T. R., Hutchings, J. B., Kaiser, M. E., & Weistrop, D. 2001, AJ, 122, 2961

Schmitt, H. R., Kinney, A. L., Hutchings, J. B., Ulvestad, J. S., & Antonucci, R. R. J. 2002, in ASP Conf. Ser. 255: Mass Outflow in Active Galactic Nuclei: New Perspectives, ed. D. M. Crenshaw, S. B. Kraemer, & I. M. George (San Francisco: Astronomical Society of the Pacific), 215

Schmitt, H. R., Storchi-Bergmann, T., & Baldwin, J. A. 1994, ApJ, 423, 237

Schulz, H., & Komossa, S. 1993, A&A, 278, 29

Scoville, N. Z., Yun, M. S., Armus, L., & Ford, H. 1998, ApJ, 493, L63

Searle, L. 1971, ApJ, 168, 327

Shaw, R. A., & Dufour, R. J. 1995, PASP, 107, 896

Silva, D. R., & Cornell, M. E. 1992, ApJS, 81, 865

Smith, H. E. 1975, ApJ, 199, 591

Stauffer, J. R. 1982, ApJ, 262, 66

Storchi-Bergmann, T. 1991, MNRAS, 249, 404

Storchi-Bergmann, T., & Pastoriza, M. G. 1989, ApJ, 347, 195

—. 1990, PASP, 102, 1359

Storchi-Bergmann, T., Schmitt, H. R., Calzetti, D., & Kinney, A. L. 1998, AJ, 115, 909

Strömgren, B. 1939, ApJ, 89, 526

Sutherland, R. S., Bicknell, G. V., & Dopita, M. A. 1993, ApJ, 414, 510

Terashima, Y., & Wilson, A. S. 2001, ApJ, 560, 139

Thurston, T. R., Edmunds, M. G., & Henry, R. B. C. 1996, MNRAS, 283, 990

Tully, R. B. 1974, ApJS, 27, 437

Vaceli, M. S., Viegas, S. M., Gruenwald, R., & de Souza, R. E. 1997, AJ, 114, 1345

Veilleux, S., & Osterbrock, D. E. 1987, ApJS, 63, 295

Vila Costas, M. B., & Edmunds, M. G. 1993, MNRAS, 265, 199

Whittle, M. 1985, MNRAS, 213, 33

—. 1992, ApJ, 387, 121

Whittle, M., Pedlar, A., Meurs, E. J. A., Unger, S. W., Axon, D. J., & Ward, M. J. 1988, ApJ, 326, 125

Wilson, A. S. 1993, in *Astrophysical Jets: Space Telescope Science Institute Symposium Series*, ed. D. Burgarella, M. Livio, & C. O'Dea (Cambridge: Cambridge Univ. Press), 121

Wilson, A. S., & Raymond, J. C. 1999, *ApJ*, 513, L115

Wilson, A. S., & Tsvetanov, Z. I. 1994, *AJ*, 107, 1227

Winge, C., Axon, D. J., Macchetto, F. D., & Capetti, A. 1997, *ApJ*, 487, L121